Delft University of Technology

Evaluation of Reduced-Order Aerodynamic Models for Transonic Flow over a Multiple-Swept Wing Configuration

Ghoreyshi, Mehdi; Aref, Pooneh; Panagiotopoulos, Anastasios; Hulshoff, Steven; van Rooij, Michel; Blom, Peter Hans Leonard; Stradtner, Mario

Evaluation of Reduced-Order Aerodynamic Models for Transonic Flow over a Multiple-Swept Wing Configuration

Mehdi Ghoreyshi* and Pooneh Aref†
U.S. Air Force Academy, USAF Academy, Colorado 80840
Anastasios Panagiotopoulos‡ and Steven Hulshoff§
Delft University of Technology Delft, 2629 HS Delft, The Netherlands
Michel van Rooij¶ and Peter Hans Leonard Blom**
NLR—Royal Netherlands Aerospace Centre Amsterdam, 1059 CM Amsterdam, The Netherlands
and
Mario Stradtner††
German Aerospace Center (DLR), 38108 Braunschweig, Germany

This study is a collaborative effort within the NATO Science & Technology Organization, bringing together multiple institutions to advance reduced-order modeling. Aerodynamic reduced-order models were developed using two pseudorandom binary sequence (PRBS) training maneuvers, where the angle of attack and pitch rate varied in a periodic, deterministic manner with white-noise-like properties. The first maneuver maintained a constant Mach number of 0.85, while the second varied Mach from 0.1 to 0.9. The test case involved a generic triple-delta wing, simulated using the DoD HPCMP CREATE™-AV/Kestrel/Kestrel tools. Prescribed-body motion was used to vary input parameters under given freestream conditions. The resulting models predicted static and stability derivatives across different angles of attack and Mach numbers. They were also used to predict aerodynamic responses to arbitrary motions, including sinusoidal, chirp, Schroeder, and step inputs, showing good agreement with full-order data. Additionally, models predicting surface pressure accurately captured upper surface pressures across different spanwise and chordwise locations for both static and dynamic conditions.

Nomenclature

A_{ref}	=	reference area, m²
CFD	=	computational fluid dynamics
C_D	=	coefficient of drag
C_L	=	coefficient of lift
C_m	=	moment coefficient
C_P	=	pressure coefficient
c	=	mean aerodynamic chord, m
f	=	frequency, Hz
M	=	Mach number
P	=	pressure, Pa
Q	=	pitch rate, rad/s
$\bar{q}$	=	dynamic pressure, Pa
q	=	normalized pitch rate, $QC/2V_\infty$, 1/rad
Re	=	Reynolds number, $\rho V_\infty/c$
SID	=	system identification
t	=	time, s
V_∞	=	freestream velocity, m/s
α	=	angle of attack, deg
β	=	sideslip angle, deg
β_j	=	regression coefficients
ρ	=	density, kg/m³
ω	=	angular velocity, rad/s

*Research Scientist, High Performance Computing Research Center, USAFA/DFAN; mehdi.ghoreyshi.Ctr@afacademy.af.edu. Associate Fellow AIAA (Corresponding Author).
†Aerospace Research Engineer, High Performance Computing Research Center, USAFA/DFAN.
‡M.Sc. Student, Faculty of Aerospace Engineering
§Assistant Professor, Faculty of Aerospace Engineering.
¶Junior R&D Engineer, Department of Flight Physics and Loads.
**Senior Scientist, Department of Flight Physics and Loads.
††Research Scientist, Institute of Aerodynamics and Flow Technology, Lilienthalplatz 7.

I. Introduction

THERE is a growing interest in using computational aerodynamics in aircraft conceptual design. At their highest practical accuracy, the unsteady Reynolds-averaged Navier–Stokes (URANS) equations can effectively predict the underlying flow physics and capture the unsteady, nonlinear aerodynamics of air vehicles across various flight conditions and flow speeds. The main limitation to using URANS or "physics-based" simulations in a multidisciplinary design approach is the computational expense. For example, performing stability and control (S&C) analysis over an aircraft's flight envelope requires aerodynamic data for tens of thousands of different states to encompass all angles of attack, sideslip angles, aircraft speeds, control surface deflections, and the time rates of Euler angle changes. This is unfeasible with a brute-force approach. If it were possible to create reduced-order models (ROMs) that maintain accuracy with only hundreds or even tens of simulations, this would allow for the early-stage simulation of a real aircraft, including all multidisciplinary interactions across the entire flight envelope, and deliver data with the accuracy necessary for development and certification [1].

ROMs offer a concise representation of unsteady flow dynamics using a limited number of spatial/temporal modes, typically fewer than 100, in contrast to the extensive number of grid points present in full-order models, which can range from 5 to 50 million or more [2]. This allows ROMs to swiftly predict responses to various inputs compared to the time-consuming computations required by full CFD solutions. Various ROM techniques are available, including indicial response methods [3], proper orthogonal decomposition (POD) [4–6], Volterra theory [7], neural networks (NNs) [8], and machine learning (ML) approaches [9,10]. System identification

falls within the realm of reduced-order modeling, yet it is distinct in its dedicated focus on constructing precise models derived from observed data. Some methods include regression methods [11], state space representations, transfer functions, the autoregressive with exogenous input (ARX) model [12,13], surrogate-based recurrence framework (SBRF) [14,15], radial basis functions (RBF) [16], and NN methods [17,18].

In this article, two input signals with either a constant or varying Mach number are investigated in connection with the generation of different ROM approaches to evaluate their prediction capabilities in two different scenarios. First, the prediction of aircraft performance and S&C characteristics for generic, prescribed maneuvers at transonic conditions. Second, the prediction of surface pressure distributions to evaluate ROM prediction capabilities in terms of aircraft load prediction using the same set of maneuvers. Such generic CFD-based maneuver simulations for training and reference data generation as well as ROMs are employed for the Future Fighter Demonstrator (FFD) use case of the NATO Science & Technology Organization research task group AVT-351 [19]. The reduced-order modeling or SID task includes the definition and computation of a training or input signal [20], the selection of a mathematical model (such as the order of regression parameters), and the choice of modeling techniques that yield the best fit to the observed data (e.g., number of neurons and hidden layers) [21]. Input signals include two pseudorandom binary sequence (PRBS) motions. During these maneuvers, the angle of attack and pitch rate change in a periodic and deterministic manner characterized by white-noise-like properties. Typical PRBS signals include sudden input variations between two distinct values, such as minimum and maximum angles of attack. However, the signals used in this article were modified to have the step changes depend on time. In the first motion, the aircraft undergoes a signal at a constant Mach number of 0.85. Upper surface pressure data were recorded for six spanwise sections. In the second motion, the Mach number varies in an optimized manner from 0.1 to 0.9. All simulations were run using the DoD HPCMP CREATE™-AV/Kestrel simulation tools. A prescribed-body motion was used to vary input parameters under given free-stream conditions (Mach number and angle of attack). Using these input signals, different ROM techniques were investigated to approximate the full-order aerodynamic model.

The rest of the article is structured as follows: First, the reduced-order modeling methods are described. Then, details on the test case, computational grids, and the flow solver are provided. Following that, results for the prediction of forces and moments from various signals, including predictions of new signals, are presented. Subsequently, ROMs are introduced for predicting surface pressure data. Finally, conclusions are drawn of this joint effort within the NATO Science & Technology Organization research task group 351.

II.   Reduced-Order Aerodynamic Models

In this article, the United States Air Force Academy (USAFA) used models based on regression and a feed-forward neural network approach, whereas The German Aerospace Center (DLR) employed a surrogate-based recurrence framework, both to predict integrated forces and moment coefficients. Delft University and the Royal Netherlands Aerospace Center (NLR) utilized long short-term memory (LSTM) neural network models in combination with enriched proper orthogonal decomposition (ePOD) to predict the sectional surface pressure data as a function of angle of attack and pitch rate. All input signals were simulated by USAFA using the CREATE™-AV Kestrel software developed by the DoD High Performance Computing Modernization Program (HPCMP) [22]. Table 1 provides a summary of all tested models, the signals used, and the corresponding output data.

Before introducing the reduced-order models, it is useful to define the following terms:

1) Static: Describes aerodynamics under steady conditions, where forces and flow remain constant over time without variation.

Table 1   Reduced-order models employed by the different organizations on either constant or varying Mach number test scenarios

Organization	Method	QoI	PRBS1 at $M = 0.85$	PRBS2 at $M = [0.1, 0.9]$
USAFA	SID	C_L, C_D, C_m	X	X
	FFNN	C_L, C_D, C_m	X	X
DLR	SBRF	C_L, C_D, C_m	X	
USAFA	FFNN	C_p	X	
NLR, TU Delft	ePOD + LSTM	C_p	X	

2) Quasi-Steady: Refers to scenarios where aerodynamic forces and moments evolve gradually, allowing the system to be approximated as a sequence of instantaneous steady states.

3) Dynamic (Unsteady): Characterized by rapidly changing flow conditions, where unsteady phenomena such as vortex shedding, flow separation, and wake interactions significantly influence the aerodynamics.

A.   System Identification

SID is dedicated to creating mathematical models that can accurately describe system behavior. According to Galrinho [23], the SID process comprises four steps: 1) system excitation for data collection, 2) selection of model structures, 3) training the models and selecting the best one from the candidates, and 4) model validation. SID models are classified into three types: gray-box models, which are built on partial system knowledge; white-box models, which are based on statistical analysis of observations; and black-box models, which are created solely from data. This article describes a gray-box identification approach based on linear, static regression to model the FFD aerodynamics at different flight conditions. The model is called gray box because it was assumed that there was a regression model or relationship between the aerodynamic coefficients and input parameters. This model is assumed to be quasi-steady since the output depends only on the present inputs, without considering past inputs. A least-squares error will then be used to estimate the model unknowns.

In more detail, a functional relationship (e.g., a polynomial) is assumed between forces and moments and the input parameters. A forced motion (i.e., a training maneuver) is then used to estimate the model unknowns. The model accuracy depends on the type of forced motion and input parameter excitation. Forced motion can be used to vary Mach number, angle of attack, acceleration terms, and angular rates in a single computation. A forced motion can be thought of as a computational flight test without kinematic restrictions (e.g., G-force) of the aircraft or pilot.

In this study, a third-order polynomial model in angle of attack was chosen for the aerodynamic coefficients at constant Mach number:

$$C_j = C_{j0} + \beta_1\alpha + \beta_2\alpha^2 + \beta_3\alpha^3 + \beta_4 q + \beta_5\alpha.q + \beta_6\alpha^2.q + \beta_7\alpha^3 \tag{1}$$

Note that for the motions of this study, $q = \dot{\alpha}$. For the motion with varying Mach number, the new model is assumed as

$$C_j = C_{j0} + \beta_1\alpha + \beta_2\alpha^2 + \beta_3\alpha^3 + \beta_4 q + \beta_5\alpha.q + \beta_6\alpha^2.q + \beta_7\alpha^3$$
$$+ \beta_8 M + \beta_9 M.\alpha + \beta_{10}M.q + \beta_{11}M^2 + \beta_{12}M^2.\alpha + \beta_{13}M^2.q \tag{2}$$

where $C_j = [C_L, C_D, C_m]$ correspond to lift, drag, and pitch moment coefficient; α is angle of attack; q is normalized pitch defined as $Q.c/(2V_\infty)$, where Q is pitch rate in rad/s, c is the mean aerodynamic chord, and V_∞ denotes freestream velocity; and M is Mach number as well. The unknowns $\vec{\beta}$ are found by a least-squares

method using the input and output data of the training maneuver. In more detail, Eqs. (1) and (2) could be written as

$$Y = \bar{\beta}.X + e \tag{3}$$

where Y is the output vector, containing all C_j data at each time step of training signal simulation; $\bar{\beta}$ is a vector of model parameters and X is a matrix of input vectors at each time step of training signal simulation; and e is the error vector between actual output and assumed model. The best set of β parameters that minimize the error is found as

$$\bar{\beta} = \left(X^T.X\right)^{-1}.X^T.Y \tag{4}$$

B. Artificial Neural Network

A feed-forward neural network (FFNN) was evaluated at USAFA to model the surface pressure data and aerodynamic coefficients of lift, drag, and pitch moments based on input signals. FFNN is one of the simplest and most used types of artificial neural networks. FFNNs are simple and easy to implement. An artificial neural network (ANN) was developed to mimic the human brain. ANN contains interconnected neurons arranged in different layers of 1) an input layer, 2) one or more hidden layers, and 3) an output layer. The information moves forward from input to hidden layers and to the output layer. Each neuron or node calculates a weighted sum of its inputs and processes the result through an activation function. The input parameters are fed into the input layer, which is the network's first layer. While multiple inputs can be used, correlated inputs may negatively impact the model's performance. In this study, the simulation data were reformatted into simultaneous, uncorrelated input data for neural network training.

Hidden layers are situated between the input and output layers. These layers contain neurons that perform a linear transformation on the input followed by a nonlinear activation function. There can be one or more hidden layers, each with a varying number of neurons. Common activation functions include rectified linear unit (ReLU), sigmoid, and tanh. The final layer, the output layer, generates the network's output. The architecture of the FFNN used in this study is illustrated in Fig. 1 for a constant-Mach PRBS signal.

The network has three inputs (α in radian, q normalized pitch rate in $1/\text{rad}$, and $\alpha.q$). For the PRBS signal with varying Mach number, additional input for Mach was added.

In more detail, FFNN consists of a single hidden layer with 10 neurons. The Levenberg–Marquardt algorithm was employed for training. Inputs are transmitted from the input layer to the neurons in the hidden layer. The signals are weighted by coefficients ω, combined with a bias term b_k, and then passed through a nonlinear activation function. The transformed signals are then forwarded to the output layer.

In this study, three different FFNNs were trained corresponding to three different outputs for lift, drag, and pitch moment coefficients. For surface pressure data, a single FFNN was trained for each spanwise position with output consisting of pressure coefficient data at different chordwise positions.

C. Surrogate-Based Recurrent Framework

An autoregressive modeling approach to account for unsteady aerodynamic effects in predicting time series of the aerodynamic force and moment coefficients is employed. In order to implement a nonlinear mapping function that approximates computationally expensive simulations into the SBRF modeling approach, a GPR model was used (see Rasmussen and Williams [24]). A software package developed by DLR, the Surrogate Modeling for AeRo-Data Toolbox in Python (SMARTy) [25], is used to integrate and apply the SBRF modeling approach. SMARTy provides various building blocks, such as regression and dimensionality reduction techniques, in a single software package. A detailed description of the development and application of the SBRF modeling approach can be found
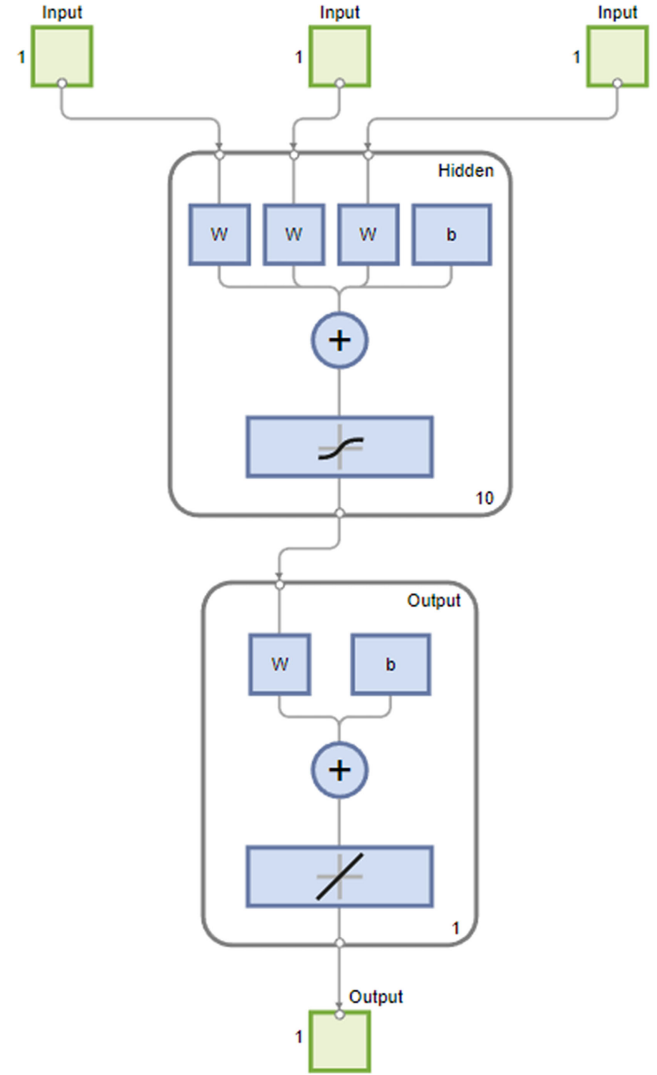

Fig. 1   FFNN used for training PRBS signal at constant Mach.

in [26]. In the following, the model architecture and its application specifics for this work are briefly described.

Considering nonlinear and unsteady aerodynamics as a discrete-time dynamic system [14]

$$\begin{aligned} \boldsymbol{x}_{t+\Delta t} &= f(\boldsymbol{x}_t, \boldsymbol{u}_t) \\ y_t &= h(\boldsymbol{x}_t) \end{aligned} \tag{5}$$

with $\boldsymbol{x}$, $\boldsymbol{u}$, y, and $h(\boldsymbol{x})$ denoting the state variables, external inputs, output quantity, and a mapping function of the system states to the output, an equivalent input/output relationship was derived. This means that the output quantity of interest at any time instance t_k depends on both the instantaneous input at time t_k and the input time history. Let the time t_{k+1} at one-step-ahead be defined as $t_{k+1} = t_k + \Delta t$, with the subscript k denoting the current discrete time step and Δt the constant time step size. According to [13], the input/output relationship accounting for time-delay history is written as

$$y(t) = \Phi\big(y_{k-1}, \ldots, y_{k-n}, u_k, u_{k-1}, \ldots, u_{k-m}\big) + \varepsilon(\boldsymbol{x}) \tag{6}$$

with a nonlinear mapping function Φ as a function of the output history and external inputs at current and past time instances. As a nonlinear mapping function, a GPR model is fitted to the training data to relate integrated coefficients for lift, drag, and pitching moment ($C_L(t)$, $C_D(t)$, and $C_m(t)$) to the model inputs. Note that a quasi-steady GPR model is fitted to initialize delayed states of the

input vector for time-series prediction. Thus, the quasi-steady GPR is inherently built and allows a comparison of a quasi-steady GPR model (QS-GPR) with the unsteady SBRF modeling approach. The SBRF model provides recursive one step ahead predictions to obtain time-series data. For static predictions, a Cauchy convergence-controlled time-series prediction at a fixed input state is employed. Stability derivative estimates are calculated based on a least-squares approach from predicted time series of sinusoidal reference motions. Note that stability derivatives refer to the set of derivatives required for stability prediction. This includes the static term at zero angle of attack, the derivative with respect to angle of attack, and the dynamic derivatives with respect to pitch rate and the time rate of change of angle of attack.

D. The ePOD-LSTM

When pressure distributions are highly detailed, the training of neural networks (NN) for their representation becomes computationally inefficient, even when including auto-encoder/decoders (see Fresca and Manzoni [27]). Therefore, an alternative is often used in which a reduced basis is first established using a truncated POD or a similar order-reduction technique, followed by the modeling of the resulting unsteady mode amplitudes using a neural network (NN). For the latter, recurrent neural networks (RNN) are often used. This approach is well described by Mohan and Gaitonde [28], as well as by Catalani [29] and Bourier [30], who consider the representation of subsonic pressure distributions using truncated POD basis combined with long short-term memory (LSTM) RNN. An additional benefit to this approach is that prediction errors can be distinguished into projection errors, i.e., a limitation from the selected truncated POD basis, and network errors resulting from, e.g., inadequate training input or network design. Moreover, the POD basis provides a boundary condition on the predicted pressure distribution.

The representation of transonic flows, however, is more challenging due to the presence of discontinuities. The accurate representation of discontinuities using a truncated POD, e.g., requires including a large number of relatively low-energy modes. Consequently, POD-LSTM reduced-order models (ROMs) must learn to describe a large number of mode amplitudes across all training datasets. This requirement escalates the training complexity of the NN, not least, because as observed by [30], an accurate prediction of temporal behavior over a range of frequencies becomes more challenging as the number of POD modes increases.

To address this problem, an alternative approach employing an enriched proper orthogonal decomposition (ePOD) is introduced here. In the ePOD, discontinuous enrichment modes are added to the reduced-order basis to represent the discontinuous parts of the pressure distribution. This allows the remainder of the data to be represented using a standard truncated POD. This dramatically lowers the number of modes needed to accurately represent pressure distributions in transonic flows. As in [29,30], the time-variant parameters of the resulting basis are modeled using an LSTM. The two main phases of this ePOD-LSTM approach are described below.

1. Model Construction and Training
a. Enriched Proper Orthogonal Decomposition. The representation of a pressure distribution using a combination of POD and enrichment modes is written as

$$C_P = \sum_{k=1}^{r} a_k(t)\phi_k(x)^T + \sum_{s=1}^{i} \phi_{e_s}(x, p(t)) + \bar{C}_p \qquad (7)$$

where r is the number of truncated spatial modes, $\phi_k(x)$ are the spatial modes with corresponding time coefficients $a_k(t)$, i is the number of shock discontinuities, and $\phi_e(x, p(t))$ are the enrichment modes with time-dependent enrichment parameters $p(t)$. $\bar{C}_P$ is the time-averaged pressure distribution, which is defined separately to allow the model to focus on the prediction of pressure fluctuations C_P^*.

The first step in defining the enrichment functions is to obtain a map of the discontinuities. Here, physics-based sensors are employed. Specifically, the gradient of the pressure fluctuations is monitored and flagged if it exceeds a specified limit (default: $(\partial C_P^*/\partial x) >= 1$). It is important to note that the raw data is first passed through a low-pass filter to smooth out high-frequency noise in the data set to prevent it from affecting the efficiency of the shock sensor. The Whittaker smoother [31] was employed with a first-order smoothing penalty of $\lambda = 10^2$. The smoothing was particularly relevant in cases where significant small-scale pressure fluctuations occur, which can impact sensor performance. Once all the locations flagged by the sensor are obtained, the shock centers are defined as the points of maximum pressure gradient, as discussed in [32].

The next step is to define the enrichment domains, i.e., the local regions in space and time within the data set where the enrichment function will be used. This is done with a user-defined constant that defines how many CFD mesh points before and after the shock location will be included in the enrichment domain. The enrichment functions are then fit to the pressure fluctuation data within the enrichment domains, as illustrated in Fig. 2.

First, a target function is defined that smoothly interpolates the C_P^* values at the start and end of the domain (here a linear function is used). The enrichment function of the form described in Eq. (8) is then fitted to the test function, which represents the difference between the C_P^* data and the target function. The parameters $p(t)$ of this enrichment mode are the amplitudes and locations of two interior control points: $\{a_1(t), a_2(t), x_1(t), x_2(t)\}$:

$$\phi_e(x, p(t)) = \begin{cases} \dfrac{a_1 x}{x_1}, & \text{for } x < x_1 \\[2mm] \dfrac{(a_2 - a_1)x}{x_2 - x_1} + \dfrac{a_1 x_2 - a_2 x_1}{x_2 - x_1}, & \text{for } x_1 < x < x_2 \\[2mm] \dfrac{-a_2 x}{1 - x_2} + \dfrac{a_2}{1 - x_2}, & \text{for } x > x_2 \end{cases}$$

(8)

Here, the fit is determined using a nonlinear least-squares algorithm. For the case considered below, a fixed number of two enrichment domains is used to represent the two shocks present in the data.

Once the reduced basis is obtained, values of $a_k(t)$ and $p(t)$ are determined using the $C_P^*(t)$ data. These must be matched to suitable input vector values. For the case under consideration, the input signal in the angle of attack-pitch rate sample space suggests that the derivatives of these parameters might significantly influence the instantaneous pressure distribution. Thus, an input vector is defined to include the angle of attack (AoA), the first and second time
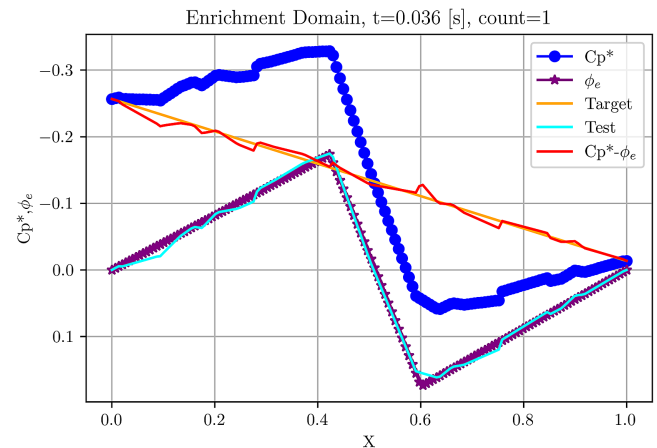

Fig. 2 Enrichment function fitting within the enrichment domain for the main shock of section 1 under the Schroeder maneuver at $t = 0.036$ s.

derivatives of AoA, the pitch rate q, and the first time derivative of q. This input vector and the $a_k(t)$ and $p(t)$ values form the data set used for the LSTM training.

b. LSTM Neural Network. Recurrent neural networks (RNNs) [33] improve on feed-forward neural networks by incorporating the output of adjacent time steps, introducing a temporal dimension to the model [34]. The network's edges that connect neighboring time steps are named recurrent edges. RNNs operate on sequences of data (e.g., time-series, time coefficients), and their weights are determined through backpropagation through time [35]. Long short-term Memory (LSTM) network was introduced by Hochreiter and Schmidhuber [36] could address the issues of vanishing or exploding derivatives and short transmission of information in standard RNNs. The LSTM architecture replaces the hidden layer of a standard RNN with a memory "cell." Each memory cell contains a node with a self-connected recurrent edge of fixed weight, creating paths through time where gradients can flow without vanishing or exploding [34,37]. A significant improvement is to make the weight on this self-loop depend on the context instead of being fixed, as proposed by Gers et al. [38]. Previous studies conducted at NLR by Catalani [29] and Bourier [30] have demonstrated that LSTM neural networks outperform other ANN or regression models in terms of accuracy for the direct prediction of POD time coefficients. Furthermore, Bourier [30] conducted a sensitivity analysis to determine the optimal hyperparameters for the baseline model. The outcomes of this analysis, combined with the findings from Catalani's study [29], were used to define the optimal hyperparameters for LSTM training in predicting the pressure distribution over different sections of the FFD model. For more details on how and why these values were derived, please refer to the respective thesis reports. The main hyperparameter values for the LSTM surrogate model are presented in Table 2.

The main difference between the previous neural network parameters and the current ones lies in the loss function. The custom loss function is a modification of the function proposed by Catalani in [29], integrated with the enrichment function. Specifically, the loss function used in training the LSTM neural network is the mean-squared error (MSE) between the projected and predicted pressure distributions. The predicted time coefficients $\{\hat{a}_k\}_{n=1}^r$ are multiplied

by the POD modes, and the predicted parameters $\hat{p}$ are introduced to the enrichment function described in Eq. (8). Consequently, the predicted pressure distribution is constructed according to Eq. (7). It is then compared to the ePOD expansion of the true targets $\{\hat{a}_k\}_{n=1}^r$ and p, as shown in Eq. (9):

$$\mathcal{L} = \frac{1}{N_x} \sum_{i=1}^{N_x} \left\| \sum_{k=1}^{r} a_k(t)\phi_k(x)^T + \phi_e(x, p(t)) - \sum_{k=1}^{r} \hat{a}_k(t)\phi_k(x)^T \right.$$
$$\left. - \phi_e(x, \hat{p}(t)) \right\|^2 \tag{9}$$

After defining the architecture of the LSTM and constructing the neural network, the final step of this stage is training the network. Considering the dataset structure and the limited overlap between the available maneuvers, the following training strategy is implemented: The Schroeder maneuver, selected for training (for details, see Sec. III), is partitioned into three datasets: training, validation, and testing. Specifically, the first 700 points are used for training, the next 250 points for validation, and the final 50 points for testing.

2. Testing Stage

In this stage of the ePOD-LSTM model, the trained LSTM neural network is employed to predict the enrichment parameters of the reduced basis for new, unseen datasets. Specifically, the model forecasts the normalized time coefficients for the ePOD modes identified during the construction of the reduced basis, as well as the parameters for the enrichment function. Using the reduced-order basis defined in the construction stage [refer to Eq. (7)], the pressure distribution can be reconstructed with the denormalized coefficients and parameters. A visual representation of the ePOD-LSTM model workflow is represented in Fig. 3.
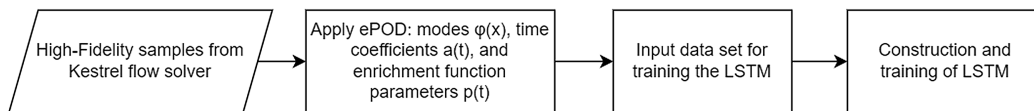
III. Training Signal Design

As mentioned earlier, the first step toward system identification is system excitation for data collection. A MATLAB code was developed at USAFA to create different signals. These signals need mean, frequency, duration, and amplitudes of inputs such as angle of attack. Pitch angles could be varied independent of angle of attack. In addition, the Mach number could be constant or changing during signal time. Minimum and maximum Mach number values are input, and the Mach could change in the form of linear, quadratic, parabolic, or optimal sinusoidal (Schroeder). Plots of input signals, input space coverage, and power spectral density are provided. For signals, the reduced frequency $\kappa = \omega.c/(2\ V)$, where $\omega = 2\pi f$, f is frequency, c is reference length, and V is freestream velocity. The MATLAB code then writes input motion data for use in Kestrel software.

Motion types include chirp (a signal with linearly increasing frequency in time), Schroeder (optimal frequency sinusoidal), sinusoidal, random, PRBS, and step signals. Some of these signals could have either a constant or a varying mean.

Table 2   LSTM neural networks hyperparameters

Hyperparameters	Values
Number of LSTM layers	2
Number of LSTM units	64
Number of dense layers	1
Number of dense units	128
Number of time steps	10
Batch size	32
Drop-out rate	0.2
Model optimization method	ADAM
Model loss function	Custom

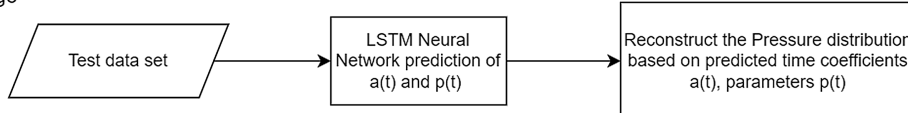Model construction and training

Testing stage

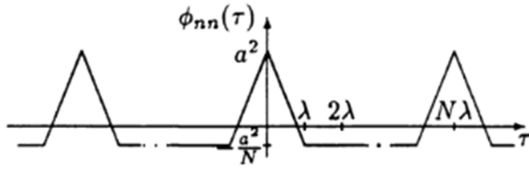**Fig. 3   The architecture of the ePOD-LSTM reduced-order model.**

Fig. 4   PRBS signal characteristics [39].

In this article, two PRBS signals are used. PRBS is a periodic signal in which the angle of attack and pitch rate change in a periodic and deterministic manner characterized by white-noise-like properties. Typical PRBS signals include sudden input variations between two distinct values, such as minimum and maximum angles of attack. However, the signals used in this article were modified to have the step changes depend on time.

A PRBS signal example is shown in Fig. 4. The maximum possible period for a maximum length sequence N is

$$N = 2^m - 1 \tag{10}$$

where m is equal to the number of shift register stages (or shifts). In Fig. 4 of Ref. [39], λ is the shifting time or the duration of the shortest impulse, and a is the PRBS amplitude. Note that λ and m should be carefully selected; one criterion here is to have a reduced frequency of less than 0.01 for a quasi-steady state assumption. The power spectral density of the PRBS signal shows that all frequencies up to $\omega_{max}\lambda/2 = \pi/4$ are excited; ω_{max} is related to the shorter time constant T_{min} by

$$\omega_{max} = \frac{3}{T_{min}} \tag{11}$$

Therefore, $\lambda = \pi/6T_{min}$. In this study, a PRBS signal was designed for 4 s with a mean angle of attack of 10° at a constant freestream Mach number of 0.85. The amplitude a increases linearly from 0 to 10° for the first half of the motion and then linearly falls to 0 for the second half of the signal. The number of shifts was set to 4. The number of shifts [denoted as m in Eq. (10)] corresponds to the number of stages (flip-flops) in the linear feedback shift register that generates the PRBS signal. The designed PRBS signal, named PRBS1 in this article, and its input parameters are shown in Figs. 5a, 5c, and 5e. The PRBS1 signal was designed for the FFD test case at Mach 0.85. Figure 5a shows the angle-of-attack variations with time. Note that the vehicle is set at a wind vector with a 10° angle of attack. Pitch angle is zero, and it varies as $\alpha(t) - 10$, where $\alpha(t)$ values are given in Fig. 5a. In this way, the pitch rate and the time rate of changes in angle of attack are the same. Figure 5c shows angle of attack in degrees versus pitch rate in deg/s. Note that the signal's maximum frequency and hence the pitch rate were limited to have a maximum reduced frequency of 0.01 for quasi-steady aerodynamic behavior. Figure 5c shows that the PRBS signal has excellent coverage of $\alpha - q$ input space. Figure 5e shows the $\alpha - \ddot{\alpha}$ space coverage of the PRBS1 signal, where $\ddot{\alpha}$ data are given in $°/s^2$ units. Figure 5e shows a large range of changes in $\ddot{\alpha}$, though most points are located at the center of the plot.

Following this, a new PRBS signal of similar design was generated. Unlike the previous signal, the Mach number in this one is not constant at Mach 0.85 but changes between 0.1 and 0.9. For Mach variations, a Schroeder signal was designed. This signal was generated from optimization of amplitude and frequency spectra of multisines. The frequency range was selected to have a reduced frequency range of 0.002–0.01.

According to Morelli [40], a Schroeder signal has excellent frequency content and a low peak factor, a measure of the ratio of maximum input amplitude to input energy. In comparison to a chirp signal, Schroeder provides better input for the frequency domain identification. The new PRBS signal is named PRBS2 in this article and is shown in Figs. 5b, 5d, and 5f. Another difference with PRBS1 is that the PRBS2 signal duration was extended to 6 s, as shown in

Fig. 5b. Because of a longer duration, the pitch rate values are smaller compared with the PRBS1. This is shown in Fig. 5d. The Mach number follows a Schroeder signal, which has a series of multisines to cover the Mach range of 0.1–0.9. Mach number variations are shown in Fig. 5f.

In more detail, Fig. 6 shows the PSD analysis of the signal and its periodogram. As anticipated, the PRBS signal excites all frequencies equally. In addition, Fig. 6 shows reduced frequency values for the signal. The maximum reduced frequency value does not exceed 0.01 to ensure the quasi-steady aerodynamic assumption.

IV.   Test Case Description

In this study, we consider an aircraft with multiple swept leading edges, which typically exhibit rapid vortical flow topology evolution and intense flow unsteadiness throughout their flight regime. Sweep angles of the triple-delta wing are 75, 45, and 75 deg. Some associated phenomena are vortex interactions, vortex–shock interactions, and vortex breakdown that influence stability and controllability [41,42]. The test case is the FFD model, which is a generic triple delta wing configuration. Its planform is based on the baseline DLR-F22 wind tunnel model [43] as part of DLR studies on the technology assessment and a design approach of a Future Fighter Demonstrator [44]. A revision of the wing design of the DLR-F22 model by ONERA within AVT-351 [19] led to the ONER-A_DLR_M421 wind tunnel model, which serves as an FFD use case in this study [45]. In comparison with the baseline DLR-F22 model, a moderate thickness, positive camber, and twist distribution were added. This model design was utilized to investigate flight dynamic characteristics in multiple static and dynamic wind tunnel experiments at ONERA. These experimental results from [45] are used for comparison of ROM predictions at subsonic conditions. CFD and ROM studies at transonic speed were conducted by Widhalm et al. [46]. Static force and moment coefficients as well as static and dynamic stability derivatives from this CFD study are used for comparison of the results in Sec. V.

Table 3 shows the flow conditions for the two PRBS signals. Flow simulations of the PRBS1 signal are performed at transonic conditions, $M = 0.85$, and an ambient pressure of 49881 Pa and a temperature of 266.5 K, resulting in a Reynolds number of about 3 million. Note that the presence of shock waves at Mach 0.85 has been confirmed through steady pressure distribution data presented in AIAA Paper 2023-4199 [46]. A CFD visualization of the FFD at Mach 0.85 and a 16° angle of attack is shown in Fig. 7. This figure depicts surface pressure distribution along with isosurfaces of the scaled Q-criterion ($Q^* = 50$), highlighting two distinct shock locations.

Figure 8a displays the hybrid computational grid on the half model, consisting of about 40 million nodes and about 150,000 elements. The boundary layer is resolved with quadrilaterals, while tetrahedra extend from the boundary-layer edge to the far field. To better capture vortices, a refined region was specified above the model, as shown in the figure. The first off-body grid nodes all satisfy $y^+ < 1.0$ in sublayer scale. The far-field distance is set to 100 times the chord length.

In addition, tap points were defined for six spanwise locations over the upper surface of the FFD. These tap points are shown in Fig. 8b. Note that three locations were chosen to be near the wing kink locations. The y positions of these tap points are [0.05, 0.09, 0.136, 0.18, 0.22, 0.28] m. These points move with the mesh. Output data include tap coordinates and pressure coefficient data at every 200 time steps. Note that not all points are exactly located on the surface. The Kestrel option of "Closest Solution Value" was used. However, Kestrel reports a "Found" parameter with values of 0 or 1; 0 means no solution found (e.g., the point is perhaps outside the mesh domain and located inside the plane). Considering the points with a Found value of 1, there are 237, 293, 189, 161, 123, and 89 points for slices 1–6, where slice 6 is the one near the wingtip.
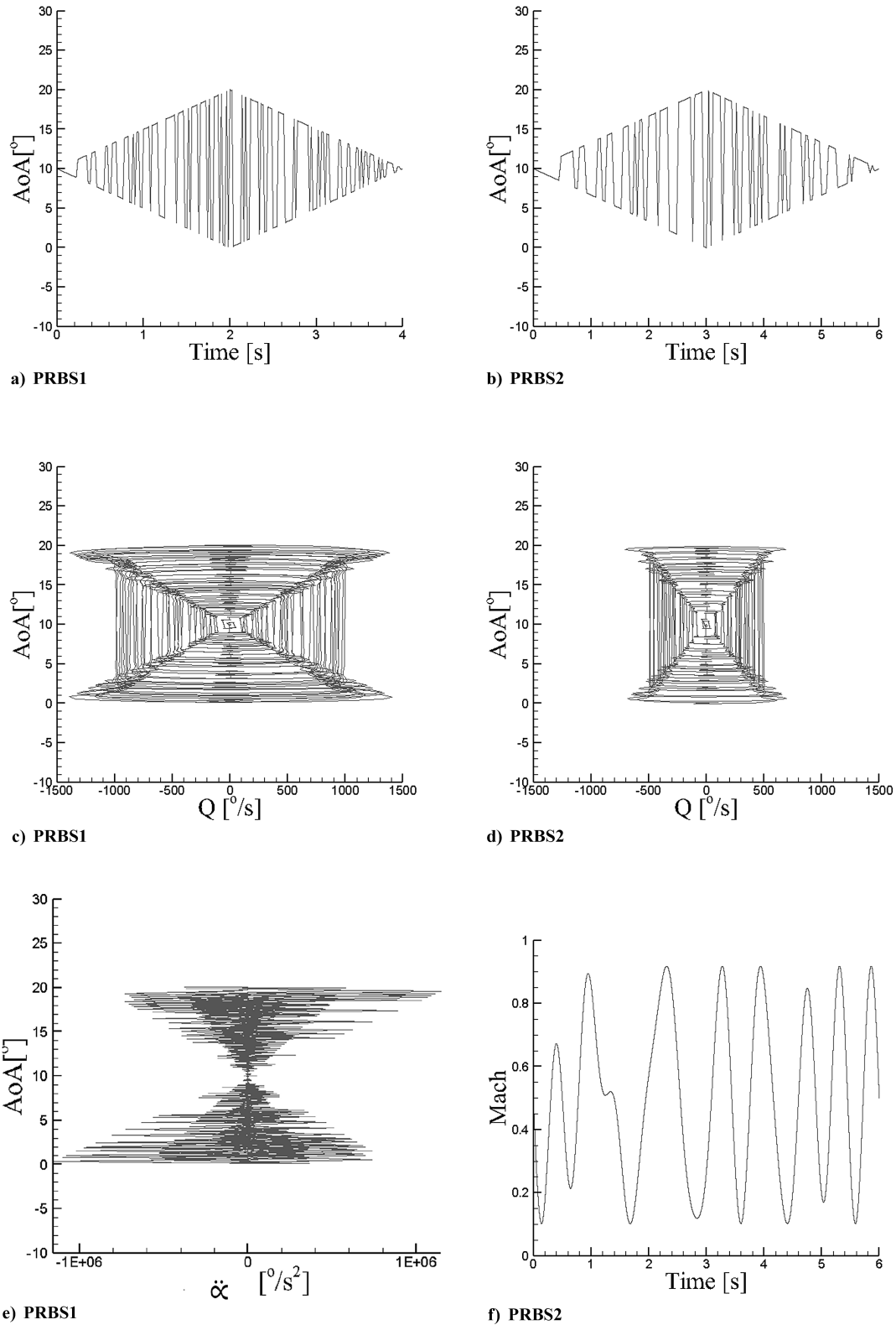
a) PRBS1

b) PRBS2

c) PRBS1

d) PRBS2

e) PRBS1

f) PRBS2

Fig. 5   PRBS1 and PRBS2 signals.

V.   Results and Discussion

All simulations were run using the Kestrel flow solver. Second-order spatial and temporal accuracy was used. The grids are half geometries with far-field, symmetry, and no-slip wall boundary conditions for the airplane. All solutions begin at a 10° angle of attack, corresponding to the mean aerodynamic angle of PRBS signals. For PRBS1, the freestream Mach number was set to 0.85 with a total temperature of 305 K and a total pressure of 305 Pa. For

the PRBS2 signal, the freestream Mach number was set to 0.4. The Mach number was then varied using a prescribed-body motion in Kestrel. In this approach, if the grid moves opposite to the incoming velocity, the relative velocity between the freestream and vehicle will increase, and hence the Mach number. If the grid moves in the direction of the freestream velocity, the Mach number will decrease. The relative velocity is set so the Mach number matches the profile shown in Fig. 5f.

Fig. 6   Power spectral density of the PRBS signal at constant Mach 0.85.

Table 3   Flow conditions for the FFD wind tunnel model

Case	α, deg	M_∞	p, Pa	T, K	Re_∞	L_{ref}, m	A_{ref}, m^2	x_r, m
PRBS1	[0–20°]	0.85	49,881	266.5	$\approx 3 \times 10^6$	0.272592	0.0807265	0.212833/0/0
PRBS2		[0.1–0.9]						

Fig. 7   CFD analysis of FFD at Mach 0.85 and 16° angle of attack.

All motions were run with a time step of 0.0002 s and eight Newton subiterations. The motions begin after 2000 startup iterations and continue for an additional 20,000 iterations for a signal duration of 4 s. Advective temporal damping was set to 0.01. The Spalart–Allmaras turbulence model with rotational/curvature correction (SARC) was used. The cost of running these signals is approximately 120,000 CPU hours using 2880 processors. Simulations were run on the U.S. DoD HPCMP Carpenter machine, which is an HPE Cray EX4000 system located at the ERDC DSRC in Mississippi. It has 1440 standard compute nodes, 4 large-memory nodes, and 8 GPU nodes (a total of 278,272 compute cores). It has 518 TB of memory and is rated at 15.75 peak PFLOPS.

A.   SID Modeling at Constant Mach 0.85

First results show the SID (regression), FFNN, and SBRF predictions using the PRBS1 signal (the signal at constant Mach 0.85). This signal was executed in Kestrel. Note that SID, FFNN, and SBRF modeling predictions depend on the chosen time step, or more specifically, on the nondimensional time step, $t^* = t.V_\infty/c$, where t is the time step in seconds. Ideally, t^* is kept about 0.01; however, this makes simulations very expensive to run. A time step of 0.0002 s was chosen for the FFD simulations at Mach 0.85.

The predicted coefficients are then rearranged according to Eq. (1), and then Eq. (4) was used to estimate the model parameters, i.e., $\beta_j, j = [0–7]$. The parameter estimation took about one or less than 1 s. In addition, three different FF neural networks were trained corresponding to C_L, C_D, C_m data of the PRBS1. Networks have one hidden layer containing 10 neurons. The Levenberg–Marquardt algorithm was used. Network training time was less than 1 minute. For the SBRF model, a reduced training set
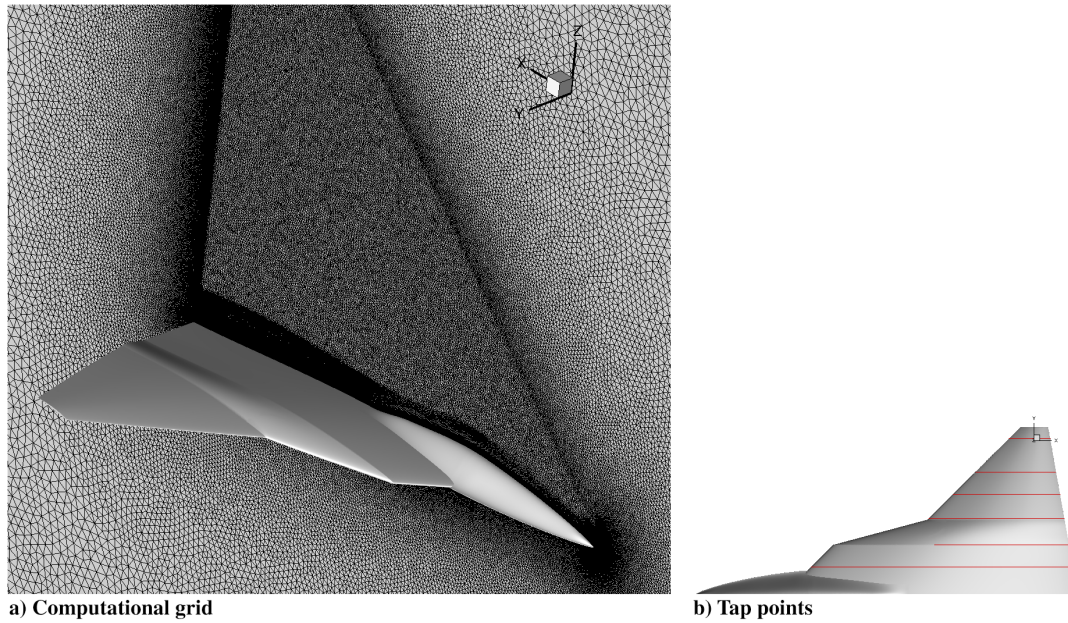
a) Computational grid   b) Tap points

Fig. 8   a) Near field of the computational grid of the generic triple delta fighter aircraft. b) Tap points at six difference spanwise slices.

was used to reduce computational cost and overfitting of the GPR model due to spatially highly correlated sample locations. The sample points were randomly split into a smaller training set consisting of about 10% of the initial size of the PRBS signal. Time-delay quantities were still computed based on the full time-series data, accounting for the original time step size. Here, no time-delayed input was considered for the two exogenous input variables α and q, but time-delayed output information is used instead to augment the input matrix with output quantities obtained at $t_k - \Delta t$ with $\Delta t = 0.002$ s. This corresponds to a time step at t_{k-10}, with k denoting the current time step. For model prediction, then $C_{j,t_{k-10}}$, for $j = L, D$, or m, is recursively fed back as model input from a single time step at $k - 10$ with k. In addition, the quasi-steady GPR (QS-GPR) model, which is inherently built when using the SBRF modeling approach, is compared to the other models. The computational cost to generate the SBRF model

(including the QS-GPR model) on the reduced sample set was less than a minute on a desktop computer.

Regression, FFNN, and SBRF models were then used to reconstruct the PRBS1 signal output based on given input changes. These model predictions of the PRBS1 signal are shown against Kestrel (actual) data in Fig. 9. Overall, a very good agreement was found by all three models at all simulation times. In more detail, the MSE values of the models are given in Table 4. MSE values are small, with the best predictions provided by quasi-steady and unsteady GPR models. These models usually provide highly accurate training data reconstruction, since only a small value as a regularization term is added to the models. Nevertheless, the choice of only using a subset of sample points as training set did not lead to an increase of model training errors. Besides these two, the FFNN model provides the best predictions for C_D. In the following, the QS-GPR model is used for comparison of model predictions at static and quasi-steady
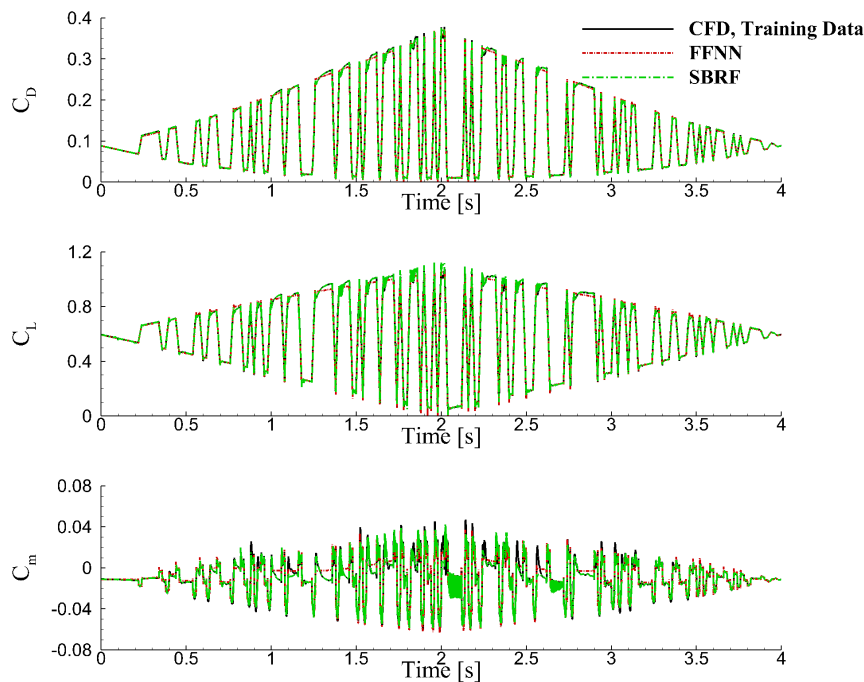

Fig. 9   Prediction of PRBS1 signal using FFNN and SBRF models.

Table 4 PRSB1 prediction mean-squared error using regression, FFNN, QS-GPR, and SBRF

Model	C_L	C_D	C_m
Regression	0.01658	0.00419	0.005722
FFNN	0.01458	0.003608	0.004487
QS-GPR	0.00025	0.00001	0.00003
SBRF	0.00029	0.00001	0.00003

conditions (such as static and quasi-steady damping stability derivative estimates), and the SBRF model for generic, prescribed maneuver predictions similar to the PRBS1 signal.

Next, the performance of the regression and FFNN models will be examined at different angles of attack. These angles were picked to cover the full range of the signal, from the lowest to the highest values. (i.e., 0–20°) with an increment of 0.5°. The way regression models are used for these predictions is by setting up the pitch rate to zero in models, i.e., $C_{jstatic} = reg_j(\alpha, q = 0)$. Likewise, in FFNN, the input columns corresponding to the pitch rate and its products (e.g., $\alpha.q$) are set to zero values. Static predictions of the FFD model at Mach 0.85 for the regression, FFNN, and QS-GPR models are given in Fig. 10. In addition, static data from Widhlam et al. [46] are used for cross-plot purposes. Figure 10 shows that both regression and FFNN predict very similar lift and drag coefficient values, and the predictions match well with those shown by Widhalm et al. for the FFD and Mach 0.85. Likewise, regression and FFNN predictions are similar for the pitch moment coefficients, with small discrepancies at some angles of attack. The predictions show the same trend as Widhalm et al. presented in Ref. [46]. However, model predictions overestimate the pitch moment data at small angles of attack and did not predict the dip seen around a 20° angle of attack in previous studies. In summary, the models do their best at the average angle of attack of the training signal, but their accuracy fades near the max and min values, i.e., [0–5°] and [15–20°] ranges.

QS-GPR predictions shown in Fig. 10 are able to capture the general trend but show minor (C_L and C_D) and large oscillations (C_m) around the mean. The SBRF model (not shown) performed similarly to the QS-GPR model. Root mean-squared error (RMSE) evaluated using the static reference data from Widhlam et al. [46] for the QS-GPR model gives values of 0.04140, 0.01112, and 0.01073 for C_L, C_D, and C_m, respectively. When evaluating the SBRF model, RMSE values of 0.03091, 0.00898, and 0.01201 are obtained for C_L, C_D, and C_m, respectively. These oscillations indicate an overfitting issue during model fit on the one hand and that probably the type of training signal is not very suitable in combination with GPR-based models. With regard to the latter, a reason might be the large step changes between two distinct angles of attack that are characteristic of the PRBS signal. Though a large range of the angular rate q is generally covered by the signal, the dataset is highly clustered with respect to the pitch rate q and almost no data is available at static conditions.

For instance, very large values are obtained during the (smoothed) step changes from one angle of attack to another, but only constant values of 5°/s and −5°/s, respectively, are obtained for the portions between the step changes. This seems to cause problems primarily for the GPR-based models.
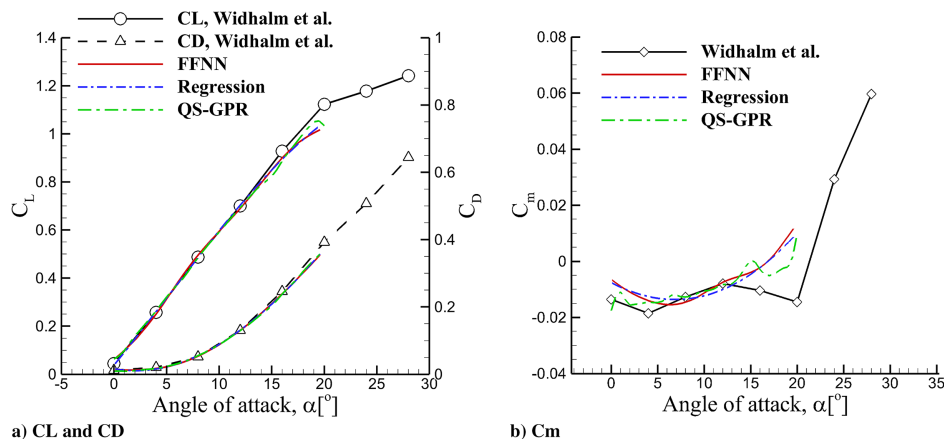
The same method used for the static case was applied to predict the curve slope with the regression and FFNN models; first, static data of $C_{jstatic1}$ are estimated for α angles. Then $C_{jstatic2}$ are found for $\alpha + 0.5°$ angles. The slope is then the difference of these values divided by a 0.5° increment. Static stability estimates from the QS-GPR were calculated based on a least-squares approach using a time-series prediction of a sinusoidal motion at a frequency of $f = 1$ Hz and an amplitude of 5°. Hence, the response to a sinusoidal motion is predicted, and the stability derivative estimation is rather a postprocessing step. Note that at mean angles of attack equal to 0 and 20°, the sinusoidal time-series prediction includes an extrapolation.

The lift, drag, and pitch moment curve slopes predicted by regression, FFNN, and QS-GPR models are shown in Fig. 11 and again compared with those reported by Widhalm et al. [46]. Overall, the trends are similar, but FFNN shows more nonlinearity in the plots than the regression and QS-GPR models. For drag, all models show the same slope and similar data to Ref. 46. For lift coefficients, the slopes predicted in the range of [5–15]° have a better match with previous data. Note that the input space is mostly covered around the mean angle of attack of 10. For the pitch moment, the FFNN provides a better match with earlier data than the regression model. The regression model exhibits a linear slope with the angle of attack and slightly overestimates in comparison to both the FFNN and previous data. The QS-GPR model also overestimates for angles from 5 to 10° and predicts a rather constant slope.

Note that discrepancies exist between ROM predictions and CFD, especially beyond a 20° angle of attack, as seen in Figs. 10 and 11. However, it is important to emphasize that these ROMs were developed using only a 4 s input signal, yet they still capture key trends in static data, slopes, dynamic derivatives, forced oscillation responses, and arbitrary motion responses with sufficient accuracy. A longer training signal could certainly improve accuracy, but it would come at the cost of increased computational effort during model development. The tradeoff between computational efficiency and predictive accuracy is a critical consideration in ROM development.

Additionally, the interpretation of discrepancies in aerodynamic predictions is often application-dependent. In the context of S&C, small differences in aerodynamic loads may or may not significantly affect handling qualities. A specialist in S&C could better assess whether the observed variations meaningfully impact control and stability predictions.

Next predictions correspond to dynamic derivatives of $CL_q + CL\dot{\alpha}$, $CD_q + CD\dot{\alpha}$, and $Cm_q + Cm\dot{\alpha}$. Note that PRBS signals used in this study have combined effects of changes in pitch rate and angle of attack because $q = \dot{\alpha}$. For isolated terms, pitch angles should be varied independent of the angle of attack. For convenience, the
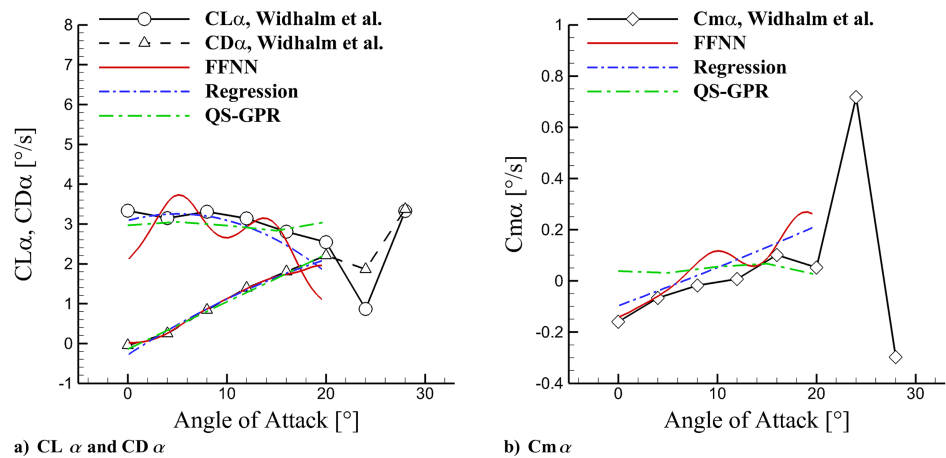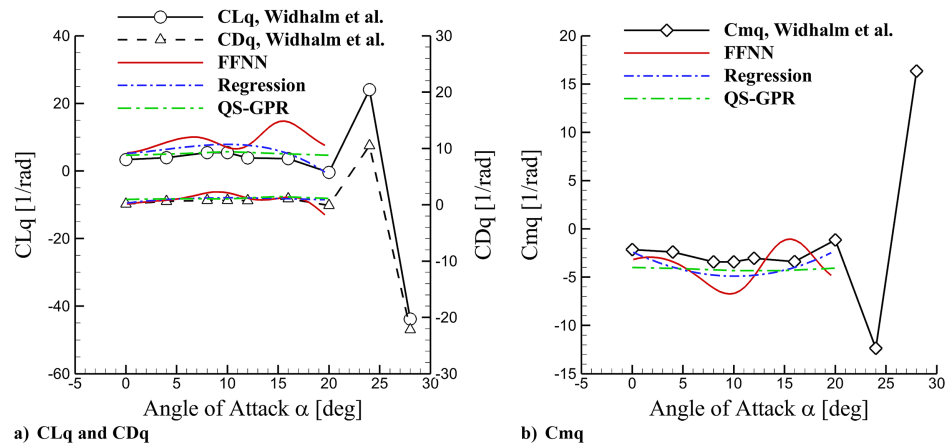

a) CL and CD   b) Cm

Fig. 10 Prediction of static data using regression, FFNN, and quasi-steady GPR models based on PRBS1 signal.

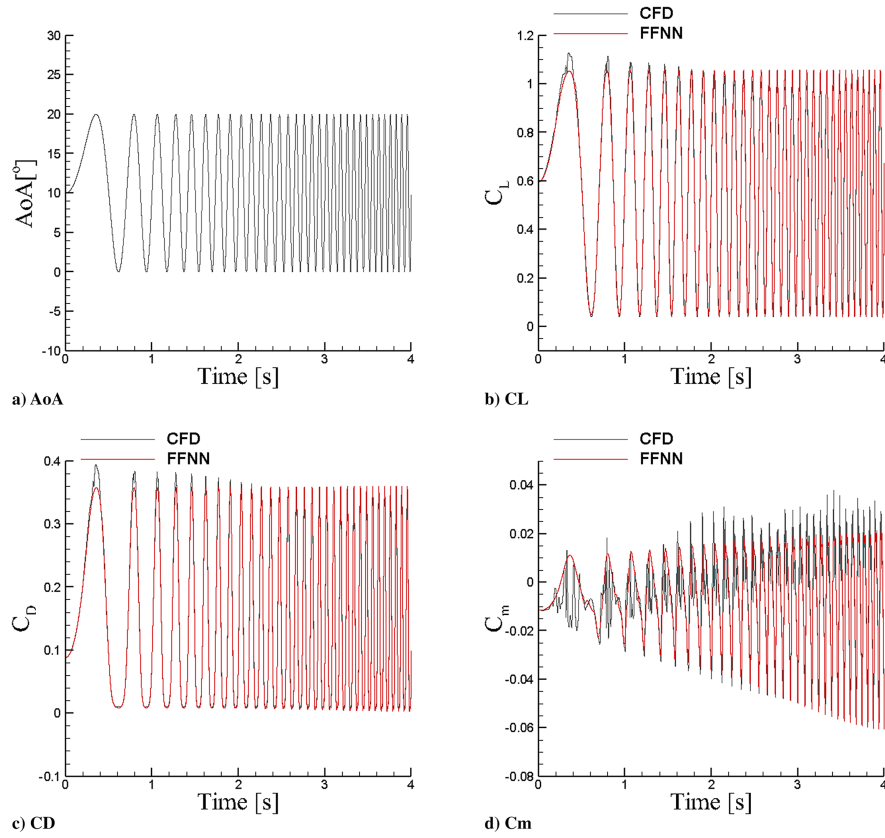**Fig. 14   Prediction of chirp with constant mean using FFNN model based on PRBS1 signal.**
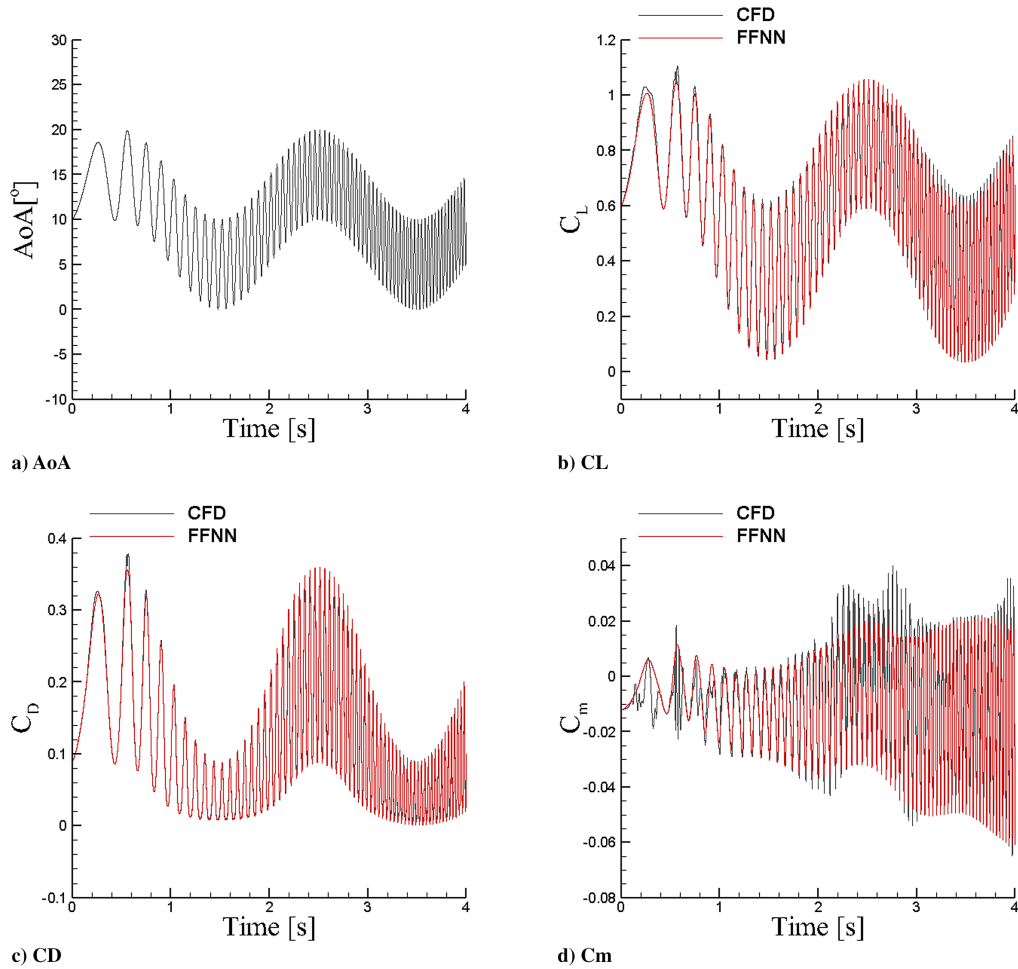

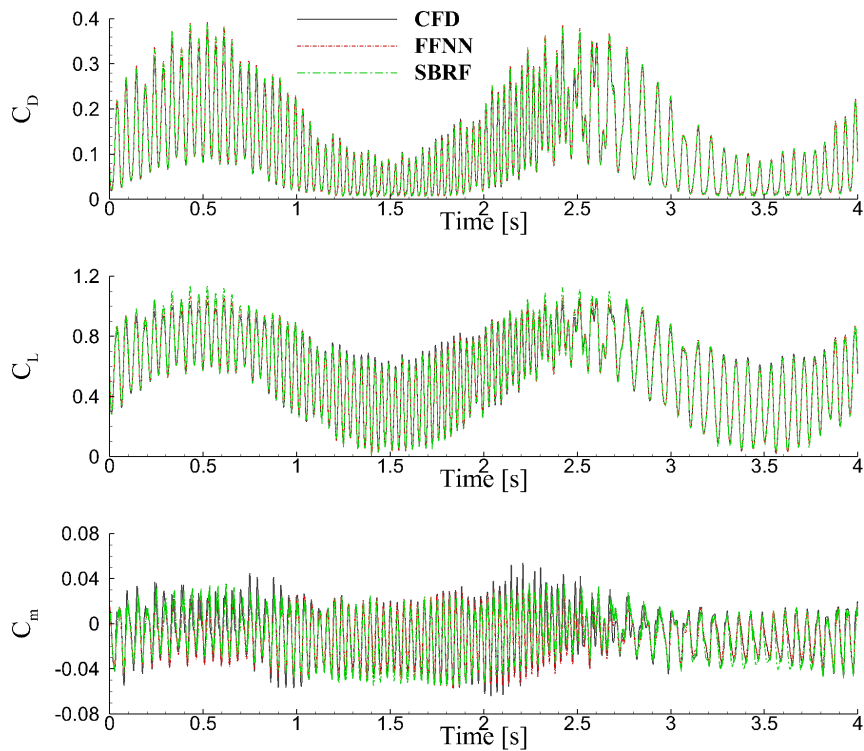**Fig. 15   Prediction of chirp with varying mean using FFNN model based on PRBS1 signal.**

Fig. 16   Prediction of Schroeder with varying mean using FFNN and SBRF models based PRBS1 signal.
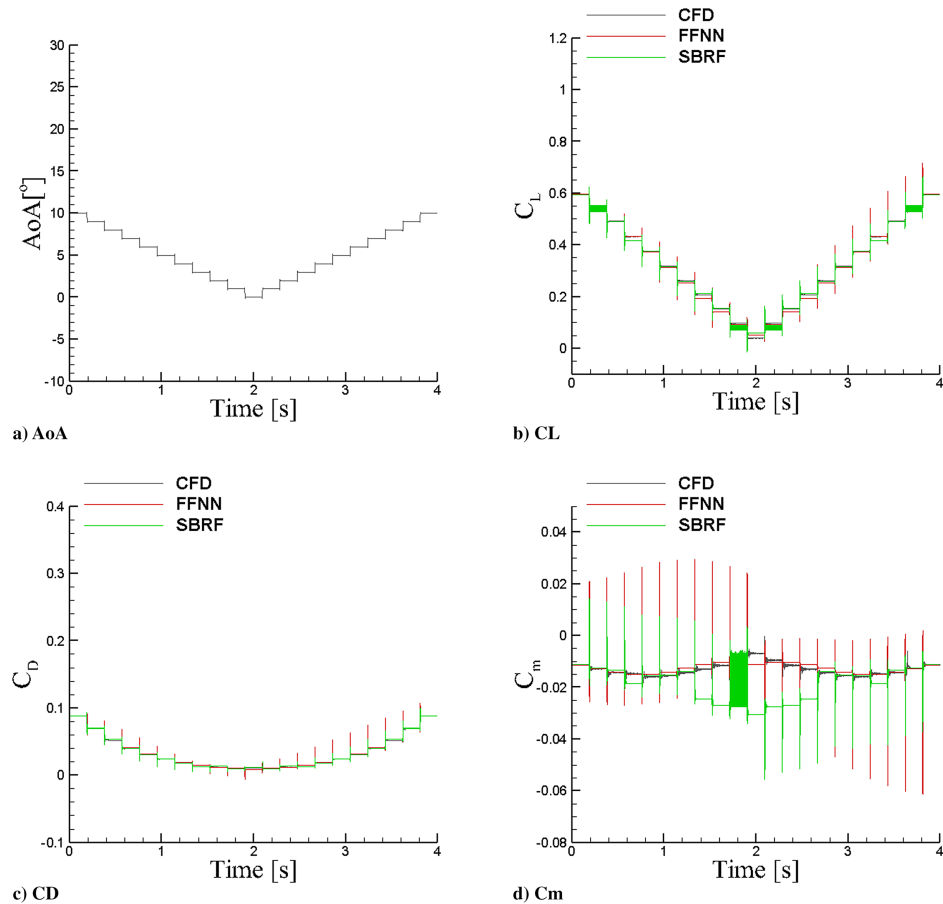

a) AoA

b) CL

c) CD

d) Cm

Fig. 17   Prediction of a step signal using FFNN and SBRF models based on PRBS1 signal.

$\dot{\alpha}$ terms are dropped, and these dynamic derivatives are named CL_q, CD_q, and Cm_q.

For prediction of these dynamic terms, models were fed with input of angle of attack and pitch rate of zero $Cj_{q0} = C_j(\alpha, q = 0)$ and at $q = 1$ rad^{-1}, i.e., $Cj_{q0} = C_j(\alpha, q = 1)$. Dynamic derivatives are the differences of these estimated terms. Note that q is the nondimensional pitch rate defined as $q = Q.c/(2V_\infty)$, where Q is pitch rate in rad/s. Regressions and FFNN model predictions of these dynamic derivatives are shown in Fig. 12 and compared with estimations using the sinusoidal time-series predictions from the QS-GPR model and those given in Ref. [46]. Overall, good agreement was found with earlier studies of the FFD at Mach 0.85. Dynamic derivatives appear to be relatively unaffected by changes in the angle of attack up to 20°. Note that the estimation of these dynamic derivatives could still be a challenging task from CFD and time-consuming using traditional pitch oscillation motions.

In addition to static and stability derivative predictions, the created model could be used for prediction of new time-accurate signals with the input space within the training signal used for model creation. One example is pitch oscillations. Different motions with combinations of the mean, amplitude, and frequency could be defined and then predicted by models. Figure 13 shows regression, FFNN, and QS-GPR model predictions of a pitch oscillation with a 10° mean angle, 5° amplitude, and frequency of 1Hz. Lift, drag, and pitch moment predictions are plotted against Kestrel data. The lift and drag show small, thin loops but a nonlinear type. The thin loops suggest that dynamic effects are relatively small, i.e., small C_{Lq} and C_{Dq} terms. The nonlinear behavior at the high angles of attack is due to vortex/shock and boundary-layer/shock interactions.

Kestrel data and model predictions match very well for lift and drag. For pitch moments, the hysteresis loop is more visible and is characterized by large nonlinearities at $\alpha = 10°$ and an eight-shaped
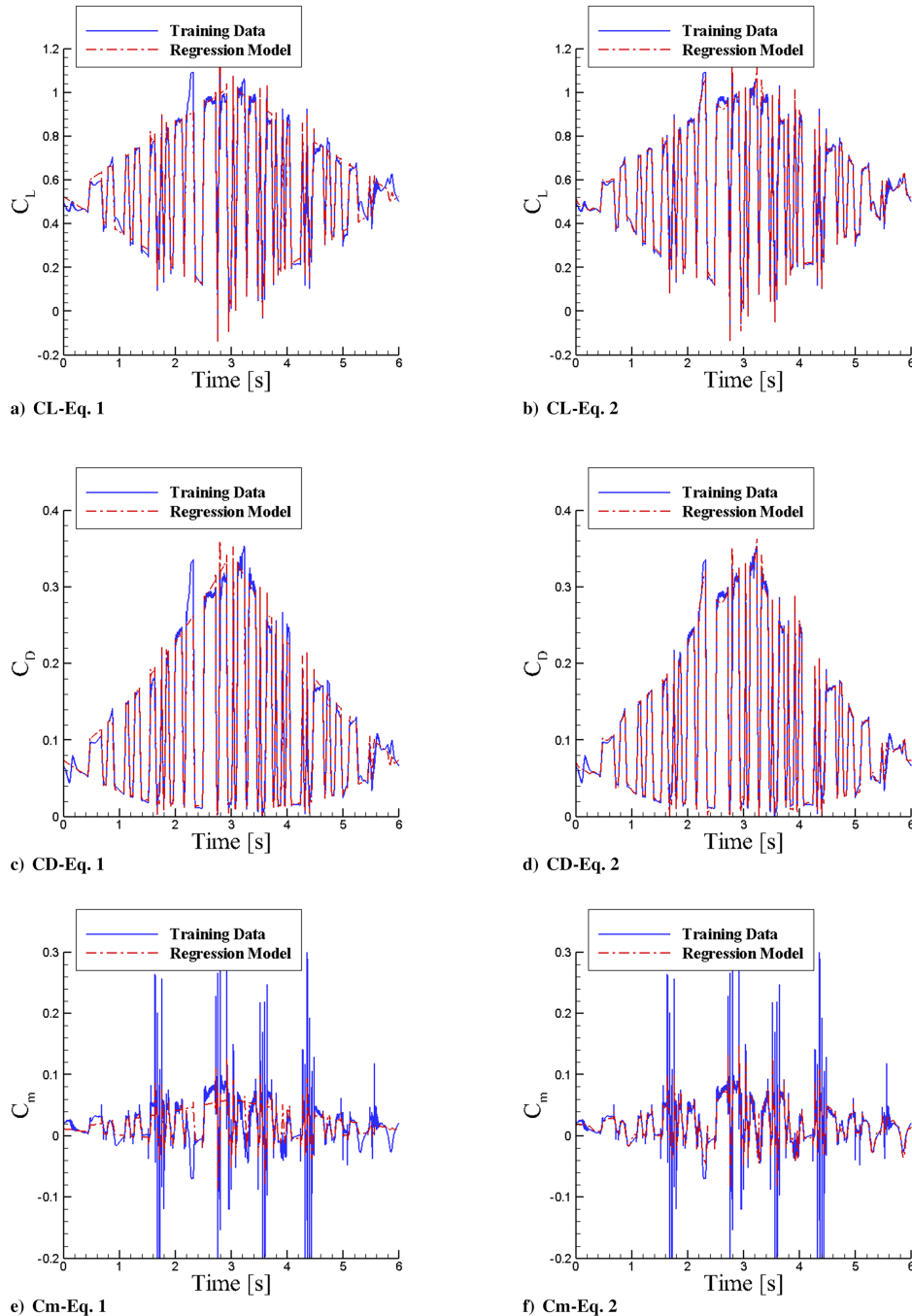

Fig. 18 Regression prediction of the PRBS2 signal using Eqs. (1) and (2).

curve around the maximum angle of attack. FFNN, regression, and QS-GPR models show discrepancies in predicting those nonlinearities. Predictions do not match with Kestrel data at all angles but are able to reproduce the general trend of the time history for C_m that was computed with Kestrel. The regression and FFNN models are generally smoother compared with the QS-GPR model, which is characterized by oscillations for some angles of attack. A reason for this discrepancy might be running this reference case at a different setup (time step, subiterations) than the training data, in addition to the previously mentioned difficulties of the QS-GPR and SBRF models in terms of poor coverage of pitch rate variations by the training data.

It should be noted that C_m is inherently more challenging to predict than lift and drag due to its sensitivity to unsteady flow structures and dynamic flow separation. While discrepancies are present, it could be argued that the results can still be considered as "comparing well" in the context of practical aerodynamic modeling. First, the model captures the key characteristics of the oscillatory motion, and both methods predict similar maximum and minimum C_m values at the mean oscillation angle. These values are critical for estimating dynamic derivatives, which are fundamental for stability and control analysis. Given that both methods lead to similar dynamic derivative values, the differences in the detailed shape of the C_m loops have limited impact on the overall predictive capability of the model in this context. Additionally, it is important to emphasize the computational efficiency of the presented approach. The pitch oscillations simulated in Fig. 13 are computationally expensive to evaluate using CFD, as numerous combinations of amplitude, mean, and frequency could be defined. In contrast, the models used in this study were trained on only a 4 s input signal yet are
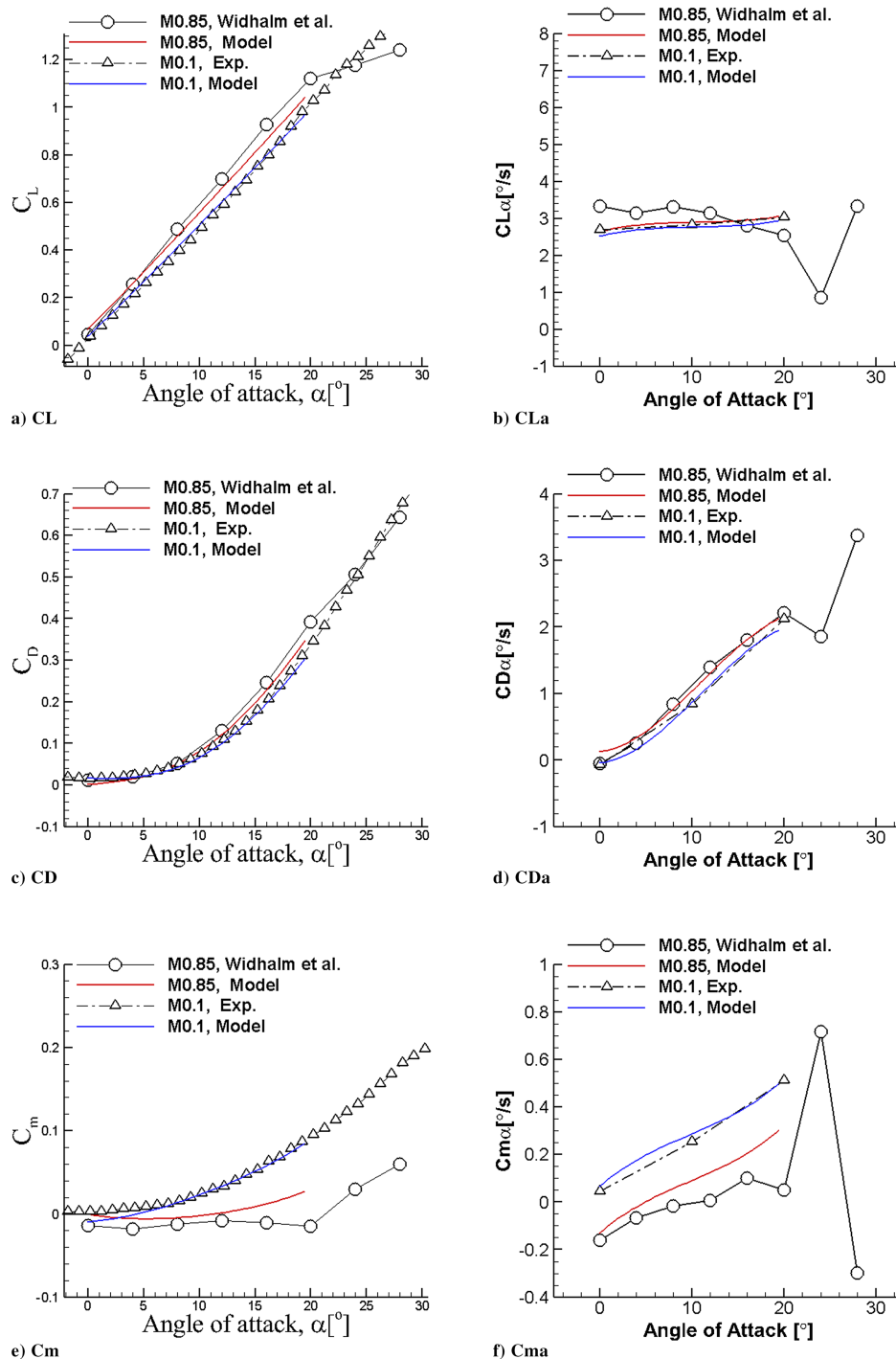

Fig. 19   Regression prediction of static and slope data at Mach 0.1 and Mach 0.85 using the PRBS2 signal.

capable of generalizing across a broad range of oscillatory motions. This provides significant cost savings while maintaining reasonable accuracy in capturing unsteady aerodynamic behavior.

In addition, FFNN was used to predict different signals such as chirp motions with constant or varying mean, Schroeder, and a step signal. For the latter two, predictions of the SBRF model were also available. Model predictions are compared with Kestrel data in Figs. 14–17. Figure 14 shows a chirp signal with a mean of 10, an amplitude of 10, and a 4 s duration. The initial frequency is 2 Hz and linearly increases with time. FFNN predictions match very well with Kestrel data. Lift, drag, and pitch moment coefficients show MSE values of 0.026, 0.0077, and 0.0087, respectively.

Figure 15 shows another chirp motion with a varying mean angle of attack. The mean angle follows a sinusoidal curve with 1 Hz frequency. The chirp has an initial 4 Hz frequency, again linearly increasing with time. FFNN predictions again match very well with

Kestrel data of this signal. MSE values are 0.022, 0.0056, and 0.0075 for lift, drag, and pitch moment coefficients, respectively. The largest discrepancy is seen at pitch moment at large angles and large frequencies.

A Schroeder signal was designed in which the mean angle of attack again follows a sinusoidal motion with 1 Hz frequency. This motion was executed in Kestrel with the same setup as PRBS1. Figure 16 compares FFNN and SBRF predictions of the Schroeder signal with time-accurate data. MSE values calculated from the FFNN model predictions are 0.024, 0.0058, and 0.0079 for lift, drag, and pitch moment coefficients, respectively. For the SBRF model, MSE values of 0.00082, 0.00003, and 0.00009 were obtained for lift, drag, and pitch moment coefficients, respectively. A good match between CFD reference and both models is observed for C_D and C_L, whereas the magnitude of C_m during the first two-thirds is not well predicted. This is improved when better coverage

a) CLq+CLadot

b) CL Sinusoidal, M0.1, f1Hz

c) CDq+CDadot

d) CD Sinusoidal, M0.1, f1Hz

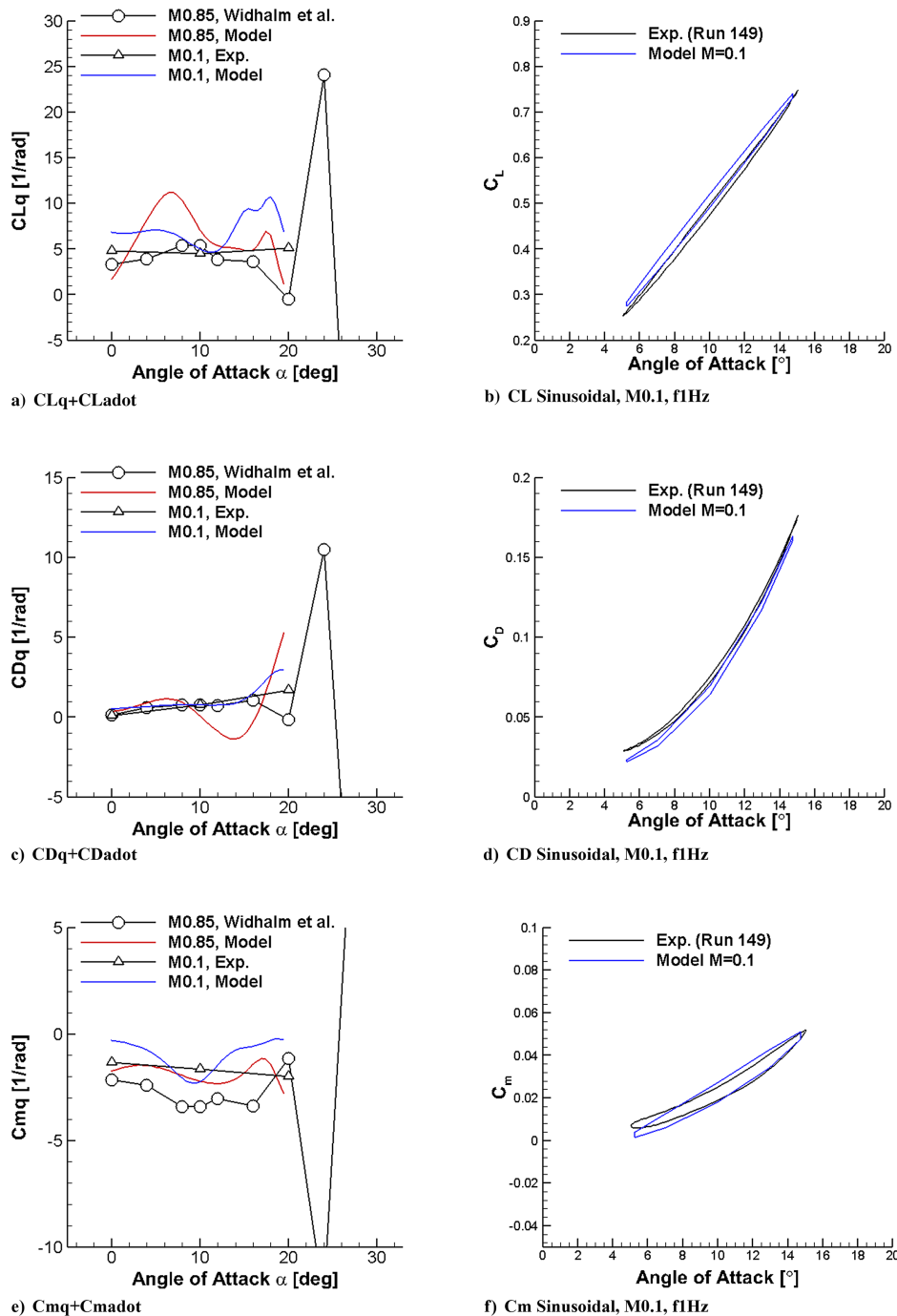e) Cmq+Cmadot

f) Cm Sinusoidal, M0.1, f1Hz

Fig. 20   Regression prediction of dynamic derivatives at Mach 0.1 and Mach 0.85 and a pitch sinusoidal at Mach 0.1 with f1Hz using the PRBS2 signal.

between training data and predicted motion exists, as can be seen for the last third of the time series at angles of attack below 15°.

Finally, Fig. 17 shows a step motion in which the signal begins at a 10 deg angle of attack. The aircraft is held at this angle for about 0.2 s and then suddenly undergoes a negative unit step, and the angle of attack drops 1 deg. The aircraft is then at a zero angle of attack at 2 s. Then, it will undergo the same motion but with a positive unit step until it reaches 10° after 4 s. All shown forces and moments have a jump in coefficients at the steps. The FFNN model predicts the static and jumps in the coefficients with reasonable accuracy with 0.0089, 0.0013, and 0.0019 MSE values for lift, drag, and pitching moment coefficients. The main discrepancies correspond to the step locations. The SBRF model shows a similar performance in terms of error metrics as for the Schroeder signal (MSE values for lift, drag, and pitching moment coefficient are 0.00013, 0.000002, and 0.00009, respectively). However, the best accuracy using the SBRF model is obtained for C_D, whereas for C_L and C_m, at some steps, a high-frequency oscillation around a constant mean with

larger deviations of the predicted mean around the minimum angle of attack is visible. Note that these oscillations are not present when evaluating the QS-GPR model, which achieves an overall similar prediction accuracy of the step motion (MSE values for lift, drag, and pitching moment coefficient are 0.00009, 0.000004, and 0.00002, respectively).

B. SID Modeling with Mach Variation

This section focuses on extending aerodynamic models to account for Mach number effects. To achieve this, the PRBS2 signal was designed to cover angles of attack ranging from 0 to 20 deg over 6 s. In this new motion, the Mach number varies between 0.1 and 0.9 following a Schroeder motion, with the initial Mach number set at 0.4. Two regression models were developed: 1) one model similar to the one used for PRBS1 using Eq. (1), with inputs of α and q; the second model is based on Eq. (2), which includes Mach number as an additional input. The predictions of these two models are compared with actual Kestrel data from running PRBS2 in Kestrel, as
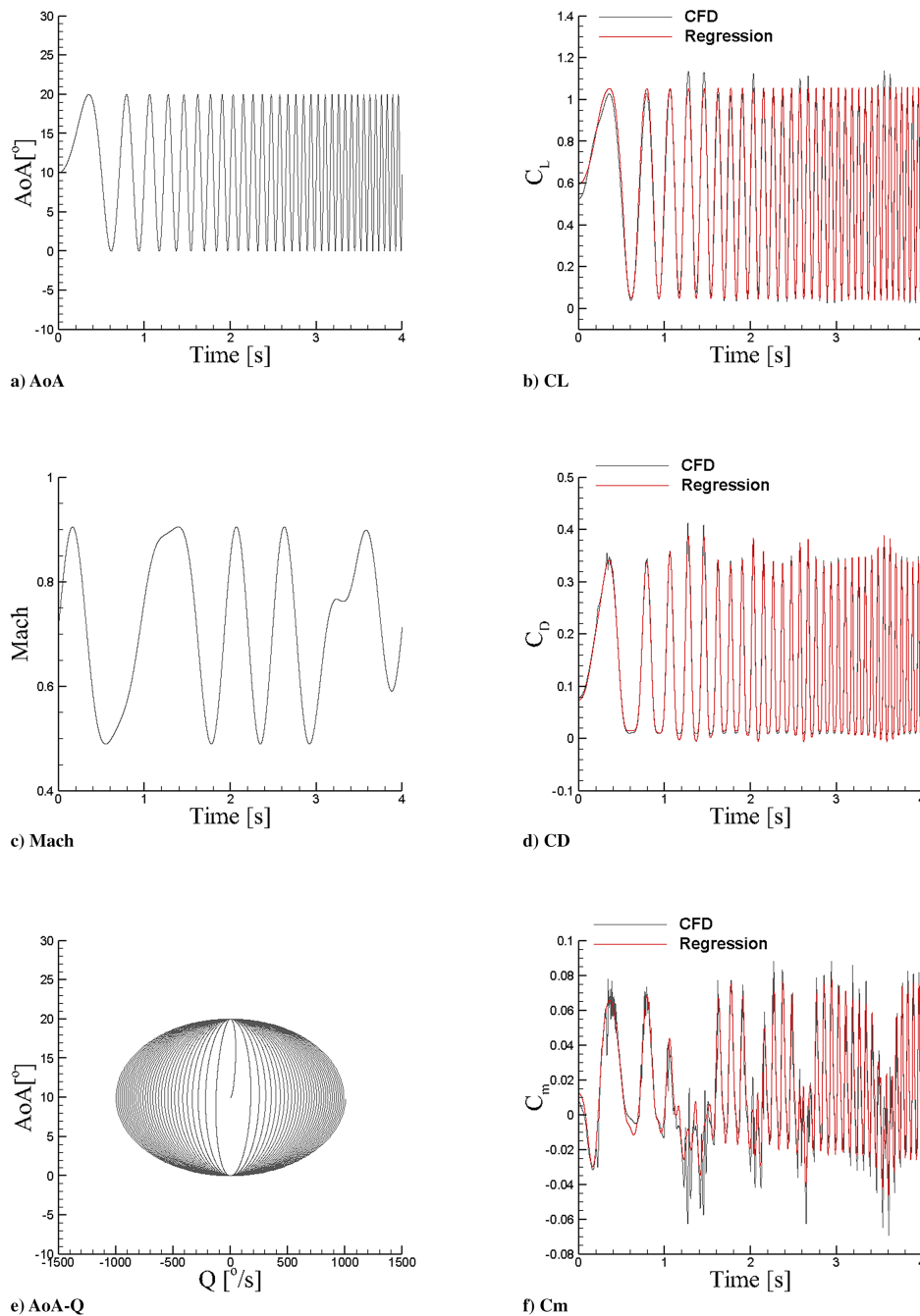

a) AoA

b) CL

c) Mach

d) CD

e) AoA-Q

f) Cm

Fig. 21   Regression prediction of a chirp motion with varying Mach number using the PRBS2 signal.

shown in Fig. 18. Using Eq. (1), models show RMSEs of 0.039, 0.013, and 0.024 for C_L, C_D, and C_m, respectively, with large discrepancies in pitch moment and coefficients at large angles of attack. However, the second model with Mach number as an additional input has MSE values of 0.02 for lift, 0.0067 for drag, and 0.017 for pitch moment coefficient. Additionally, an FFNN model was created to predict lift, drag, and force moments, using seven inputs (α, q, M, $\alpha.q$, $\alpha.M$, $q.M$, $\alpha.q.M$).

Regression models were then used to predict static and stability derivatives of the FFD at different Mach numbers and angles of attack. Figure 19 shows static and slope data at Mach 0.1 and 0.85. Previous Kestrel data at Mach 0.85 were obtained from Widhalm et al. [46]. For Mach 0.1, the ONERA wind tunnel data are plotted. Figure 19 shows that static and slope data match well with wind tunnel data at Mach 0.1 for the ranges of shown angles (this range corresponds to the signal input range). Lift and its slope curve underestimate Ref. 46 data at Mach 0.85. The same applies to drag

and pitch moment coefficient at Mach 0.85. More interestingly, model predictions at Mach 0.9 (not shown in this article) match better with previous Kestrel data at Mach 0.85. A few suggestions to improve model prediction accuracy are to refine the signal with a longer duration and to include more training data at transonic speeds than in the subsonic regime.

From the PRBS2 signal, dynamic derivatives of C_{Lq}, C_{Dq}, and C_{mq} were estimated at Mach numbers of 0.1 and 0.85. These predictions are compared against data from Ref. [46] and wind tunnel data [45] in Fig. 20. In addition, the models created from the PRBS2 signal were used to predict a sinusoidal pitch motion at Mach 0.1, with a mean angle of 10°, an amplitude of 5°, and the motion frequency of 1 Hz. The model predictions are also compared with wind tunnel data (this corresponds to test run 149 in wind tunnel documents) in Fig. 20. The predictions show that dynamic derivatives are insensitive to the angle of attack variations up to 20° for both shown Mach numbers. However, dynamic derivatives
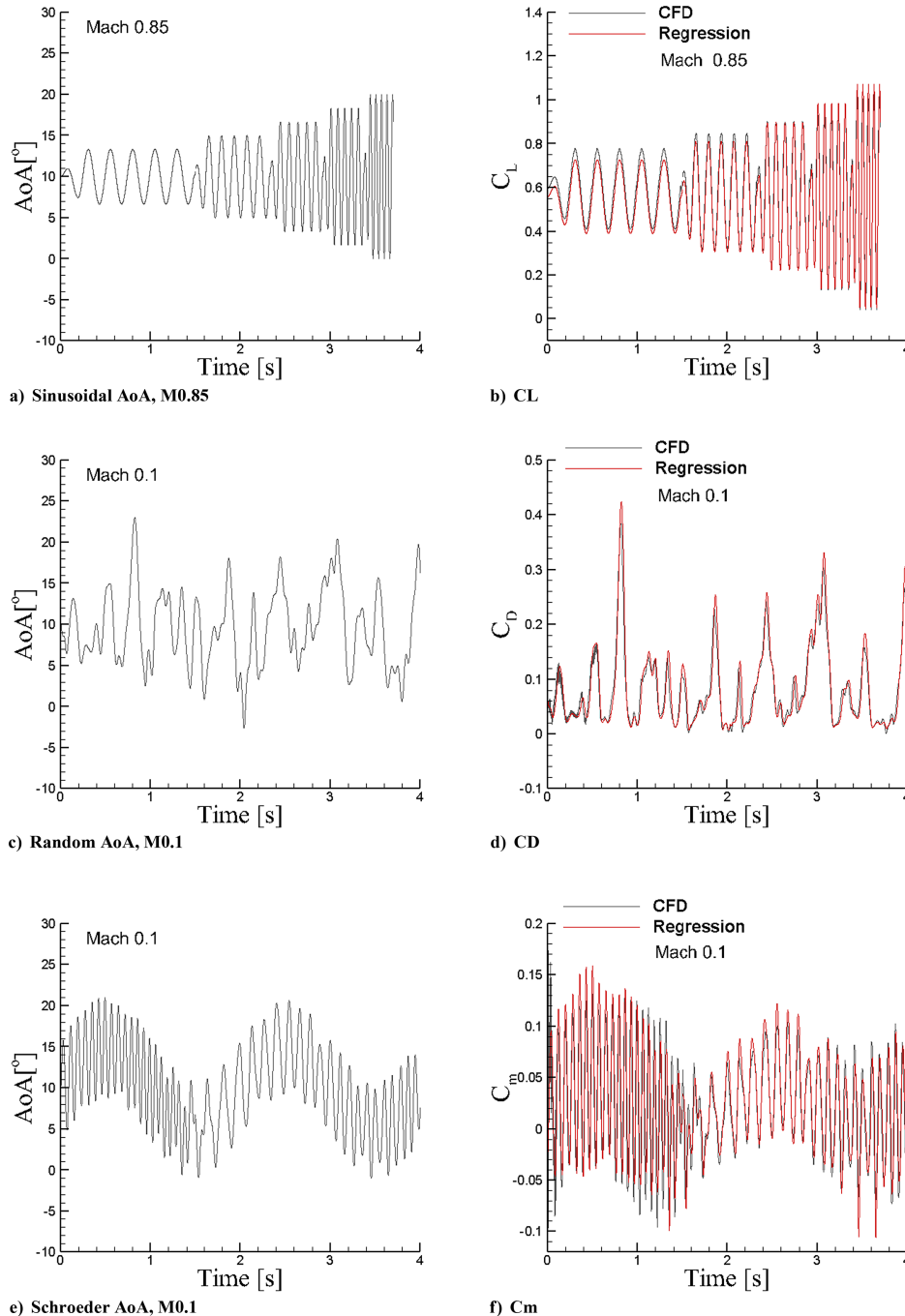

a) Sinusoidal AoA, M0.85

b) CL

c) Random AoA, M0.1

d) CD

e) Schroeder AoA, M0.1

f) Cm

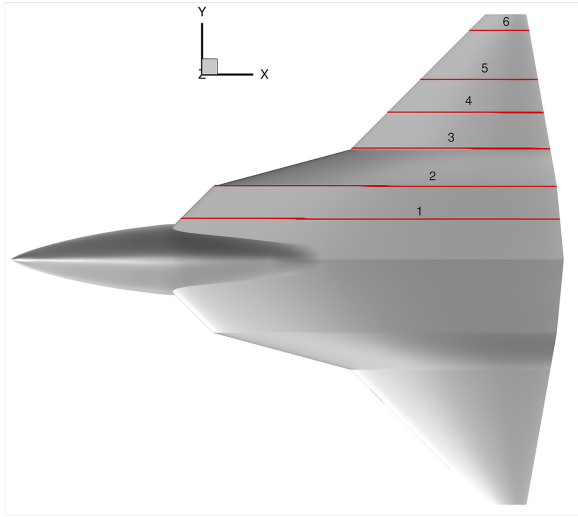Fig. 22   Evaluating the regression model for prediction of different signals using the PRBS2 signal.

Fig. 23   Pressure tap positions.
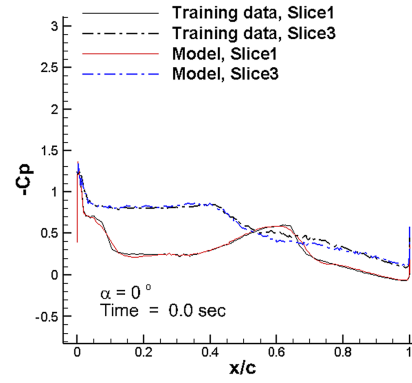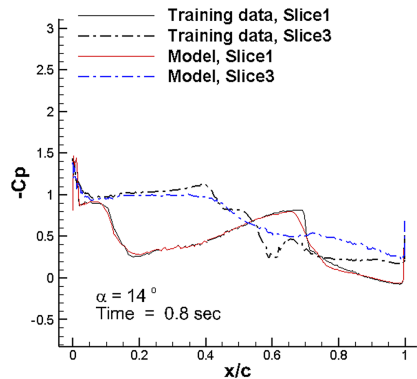
depend on the Mach number, e.g., C_{mq} becomes more negative with increasing Mach number. Figure 20 shows that model predictions fall in the range of previous and measured data. The model predictions at Mach 0.85 show the largest discrepancies. The sinusoidal predictions at Mach 0.1 match very well with wind tunnel data, though ROM performance should be compared with Kestrel rather than with measured data.

Likewise, models created for the PRBS1 signal, the new models could be used to predict the responses to new motions, even including Mach number variations. As an example, a chirp motion with linearly increasing frequency with time was defined. This motion runs for 4 s. It has a mean angle of $10°$, an amplitude of $5°$, and an initial frequency of 2 Hz. The Mach number is not fixed and varies between 0.5 and 0.9 following a Schroeder motion. This motion is shown in Fig. 21. The $\alpha - Q$ space coverage is also shown in the figure as well. Model predictions of this motion are compared with time-accurate simulation data in Fig. 21 as well. Overall, the predictions match well with Kestrel data, especially for lift and drag coefficients. Discrepancies in amplitude and phase are due to slight differences in dynamic derivative predictions. Additionally, three motions were defined at
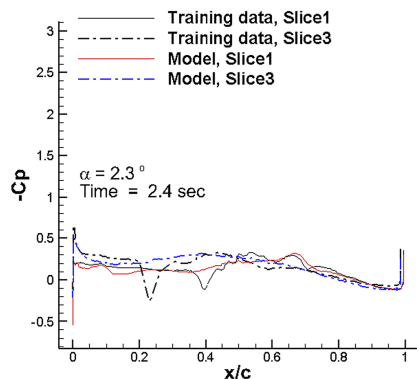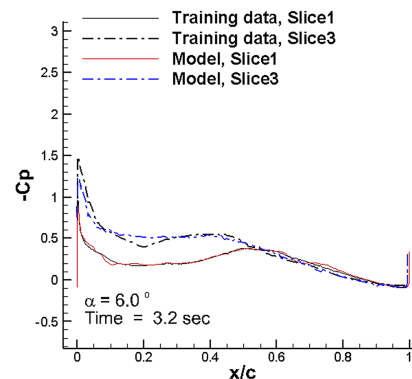

a) PRBS1 signal

b) T=0s AoA=10

c) T=0.8s AoA=14

d) T=1.6s AoA=18

e) T=2.4s AoA=2.3

f) T=3.2s AoA=6

Fig. 24   Modeling pressure data at sections 1 and 3 using FFNN. Signal is PRBS1 at Mach 0.85.

Mach 0.1: sinusoidal, random, and Schroeder. These motions are shown in Fig. 22 and have a duration of 4 s, except for the sinusoidal, which has 3.7 s. Sinusoidal is a combination of five signals of constant frequency; as time progresses, the signal frequency and amplitude increase in time. Random was generated with different amplitude and frequency combinations. Finally, a Schroeder motion was defined in which the mean angle of attack follows a sinusoidal motion with a frequency of 0.5 Hz. The motion data were fed into models, and the predictions are compared against time-accurate data in Fig. 22. Again, the overall trends were predicted well with small discrepancies at the peak values.

C. Modeling Surface Pressure Data

1. FFNN

The PRBS1 signal was run again in Kestrel, but this time with pressure tap points of Fig. 8b. This includes about 1092 data points. Note that each slice has a different number of points; those near the wing tip have fewer points than those near the root. The tap points only correspond to the upper surface sections. Tap data

are defined using coordinates of x, y, z. At every 20 time steps, pressure coefficient data at these locations are recorded. Note that the angle of attack and pitch rate vary according to the PRBS1 signal shown in Fig. 4. Data were then rearranged to have input data of $[\alpha, q, \alpha.q]$ and corresponding C_p data for each slice. Then FFNNs were used to train the models based on these data for each section. The model predictions of two slices are shown here: slices 1 and 3. These slices are shown in Fig. 23. In these figures, the PRBS1 signal, the pressure section, and the initial time C_p data are shown. FFNN models took about 1 hour to be trained due to the amount of data. These models were then saved to be used for prediction of pressure data of new signals. Model training data for slice 1 and slice 3 are shown in Fig. 24 at different time instants. In this figure, the input signal and section data from Kestrel and model predictions are shown. Depending on the angle of attack, pitch rate, and slice locations, shock waves formed over the upper surface at different chordwise locations. Figure 24 shows that models were trained to capture the shock waves and pressure coefficient values with the best accuracy. Note that slice 3 has less
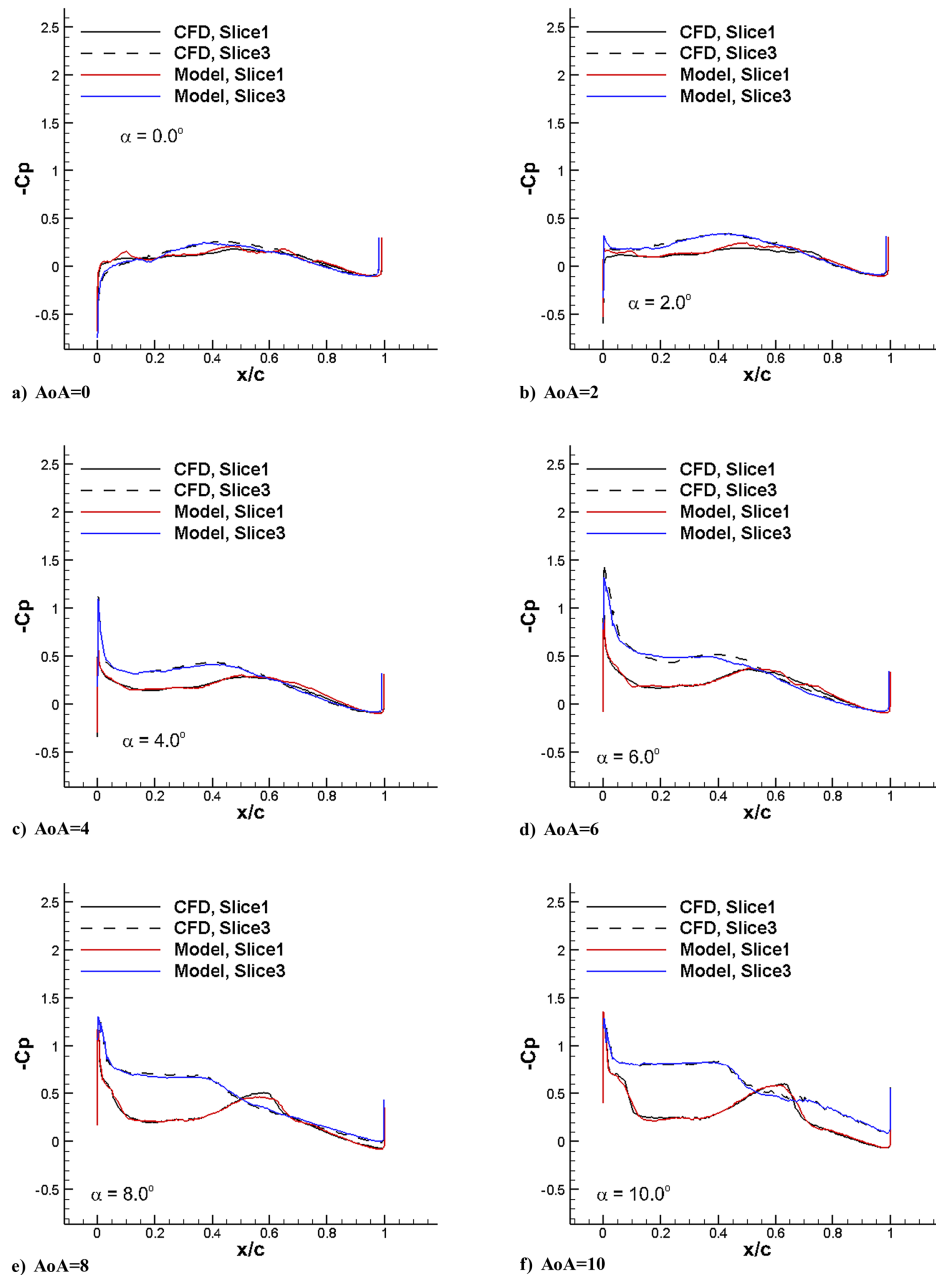

Fig. 25   Modeling pressure data at sections 1 and 3 of FFD at static angles and Mach 0.85. The model was created from the PRBS1 signal.
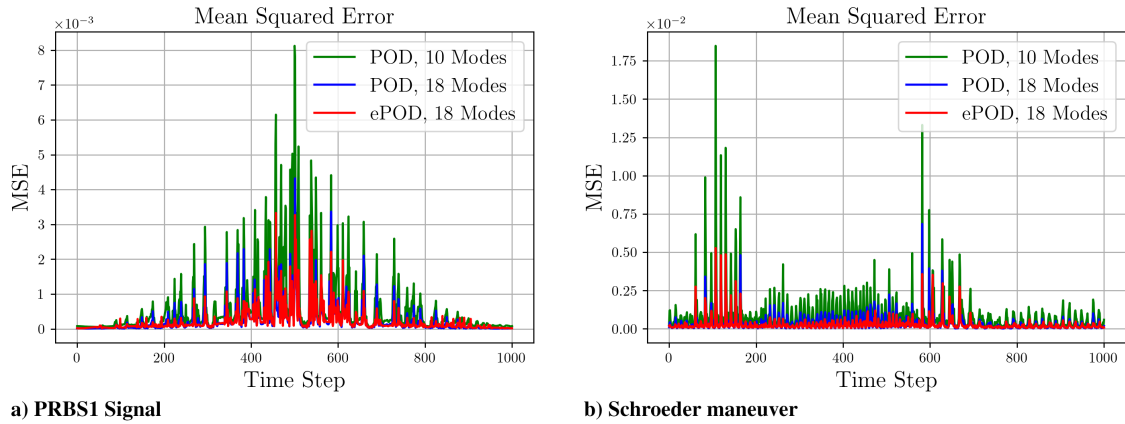
a) PRBS1 Signal

b) Schroeder maneuver

Fig. 26   Mean-squared error for the maneuvers under consideration.

negative pressure data at the upper surface than slice 1 for high angles of attack. The shock positions are visible with a sudden change in Cp values especially for angles of 10° and higher. The shock becomes stronger and moves aftward with increasing angle of attack.

The NN models were then used to predict the pressure data of a step motion shown in Fig. 17a. Note that tap data were predicted at the center of each segment; it was assumed that these data correspond to static data, as the pitch rate is zero during each step segment. Model predictions at different angles of attack at slice sections of 1 and 3 are shown in Fig. 25. C_p predictions match very well with data calculated from time-accurate simulations.
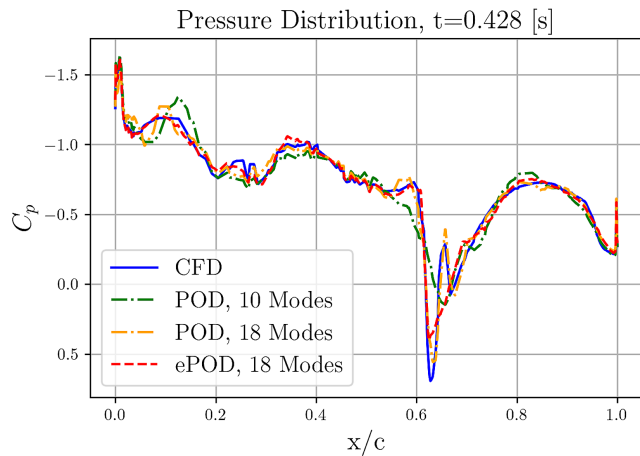

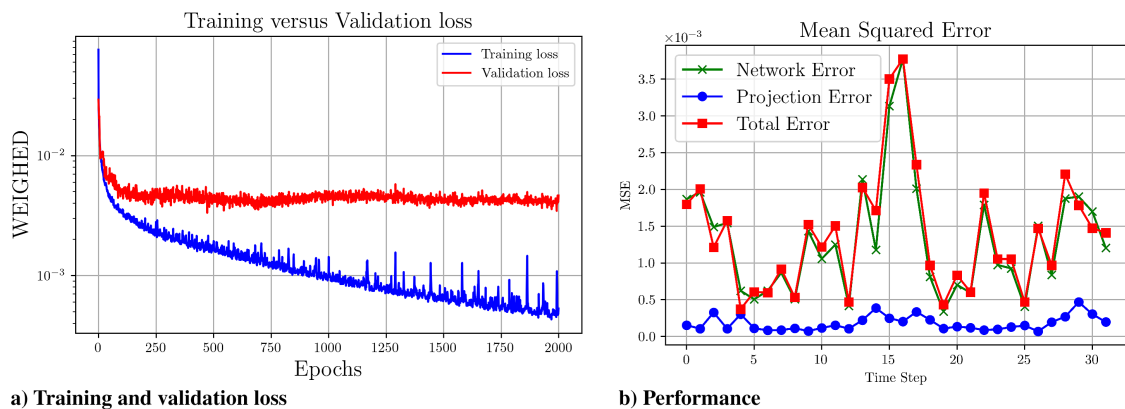Fig. 27   Comparison between enriched and standard POD, for t = 0.428 [s].

2. EPOD-LSTM

a. Projection and Training Error.   As previously discussed, the initial stage involves constructing a reduced-order basis using the proposed enriched proper orthogonal decomposition (ePOD) technique. To demonstrate the advantage of this approach over the standard method in modeling transonic flow regimes, the MSE is assessed. Specifically, the projection error of the ePOD technique is computed and compared to the corresponding error of the standard POD method using an equal number of POD modes, as well as to the total of POD modes and enrichment parameters. For instance, in the case of ePOD utilizing 10 modes and 8 enrichment function parameters (4 parameters per shock), it is compared to the standard mode using 10 modes and to the standard method using 18 POD modes. As observed in Fig. 26, the MSE for the ePOD method is consistently lower than that of the standard POD with an equivalent number of parameters across all time steps in the PRBS1 dataset. Specifically, the average MSE for the projection error of the ePOD method is $2.25 \cdot 10^{-4}$, whereas for the standard POD with the same number of parameters, it is $2.42 \cdot 10^{-4}$, and for the same number of modes, it increases to $5.74 \cdot 10^{-4}$.

Furthermore, in the case of the Schroeder maneuver, the MSE of the ePOD method generally outperforms that of the standard POD. On average, the MSE is $2.78 \cdot 10^{-4}$ for ePOD, $3.38 \cdot 10^{-4}$ for POD with the same number of parameters, and significantly higher at $8.62 \cdot 10^{-4}$ for standard POD with the same number of modes. This pattern holds true except for three specific instances in time. Further investigation into these time steps reveals that the fitting error was significant in these cases, caused by high oscillations following the shock discontinuity, which resulted in underfitting of the previously described fitting methodology, as observed in Fig. 27. Moreover, the MSE is obtained by averaging the error for the pressure distribution at each time instance. Consequently, small pressure fluctuations within the dataset contribute to this error. The proposed method is specifically designed to handle shock discontinuities, whereas the
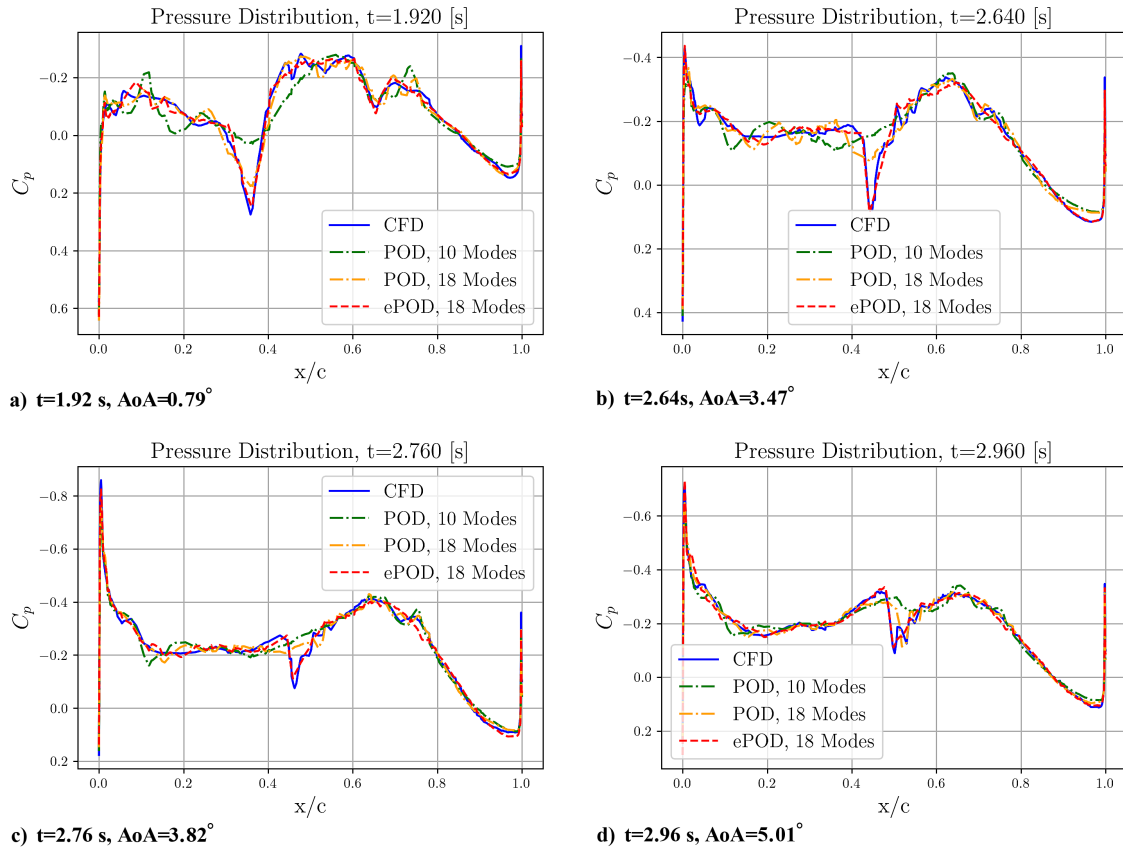

a) Training and validation loss

b) Performance

Fig. 28   a) Training and validation loss. b) Mean-squared error, between predicted, projected and true pressure distribution.

a) t=1.92 s, AoA=0.79°

b) t=2.64s, AoA=3.47°

c) t=2.76 s, AoA=3.82°

d) t=2.96 s, AoA=5.01°

Fig. 29   Pressure coefficient reconstruction of section 1 with POD and ePOD methods, for PRBS1 signal.

a) t=1.32 s, AoA=4.77°

b) t=1.36 s, AoA=3.64°

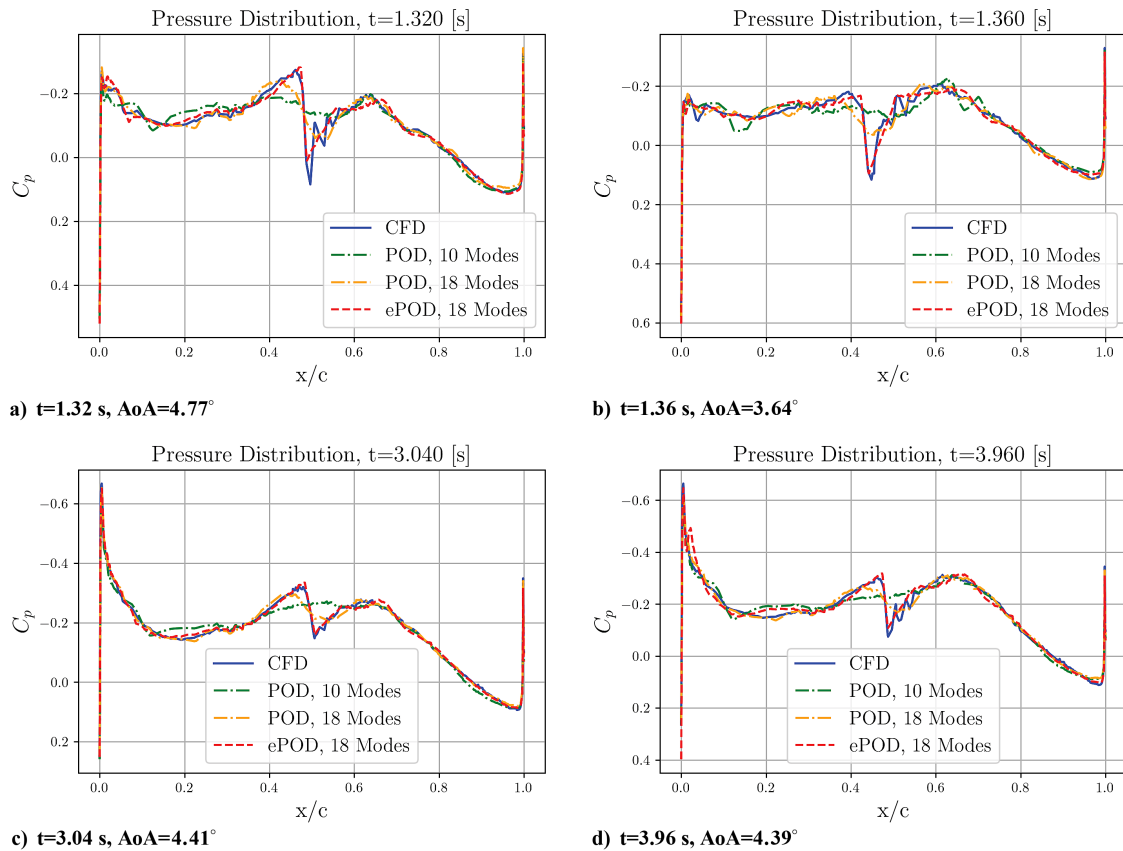c) t=3.04 s, AoA=4.41°

d) t=3.96 s, AoA=4.39°

Fig. 30   Pressure coefficient reconstruction of section 1 with POD and ePOD methods, for Schroeder maneuver.

standard POD method with more modes may better address these small pressure fluctuations in regions of the dataset where no pressure discontinuity occurs.

The following results concern the training stage of the neural network. Figure 28a presents the weighted training and validation loss for the Schroeder maneuver. In Fig. 28a, 95% of the weighted version is the contribution of loss function 9 and 5% from the mean-squared distance between the predicted and true time coefficients and parameters. The validation loss reaches a plateau of approximately $4 \cdot 10^{-3}$ after the first 400 epochs, while the training loss continues to decrease, eventually reaching a minimum of about $4 \cdot 10^{-4}$.

The pressure distribution for selected time instances for the PRBS1 signal and Schroeder maneuver are illustrated in Figs. 29 and 30, respectively. It becomes apparent that the proposed method performs remarkably well in the discontinuity region, outperforming the standard methods and facilitating the application of the model for the prediction of the pressure distribution in the transonic flow regime. Furthermore, the normalized time coefficients and the parameters of the enrichment function are depicted in Fig. 31. The normalized first and last time coefficients, along with the parameters of the second

shock (the strongest and most significant one) predicted by the neural network, are compared with the actual validation data. A particularly interesting observation relates to the frequency and periodicity of these data. By comparing the first and last time coefficients, it can be derived that as the number of POD modes increases, the frequency of the corresponding time coefficients also increases. Consequently, it becomes more challenging for the neural network to predict these highly oscillating coefficients. Thus, by utilizing the ePOD reduced-order basis, the total number of predicted parameters decreases, and the convergence of the neural network improves.

b. Testing Error.

In this section, the results from the testing stage of the ePOD-LSTM reduced-order model are presented. The predicted pressure distribution of the LSTM neural network is compared with both the actual enriched reduced-order basis and the full-order pressure distributions. To evaluate the performance of the model, three different types of errors were evaluated for the test data set.

The first error evaluated was the projection error, defined as the MSE between the enriched reduced-order basis and the full-order
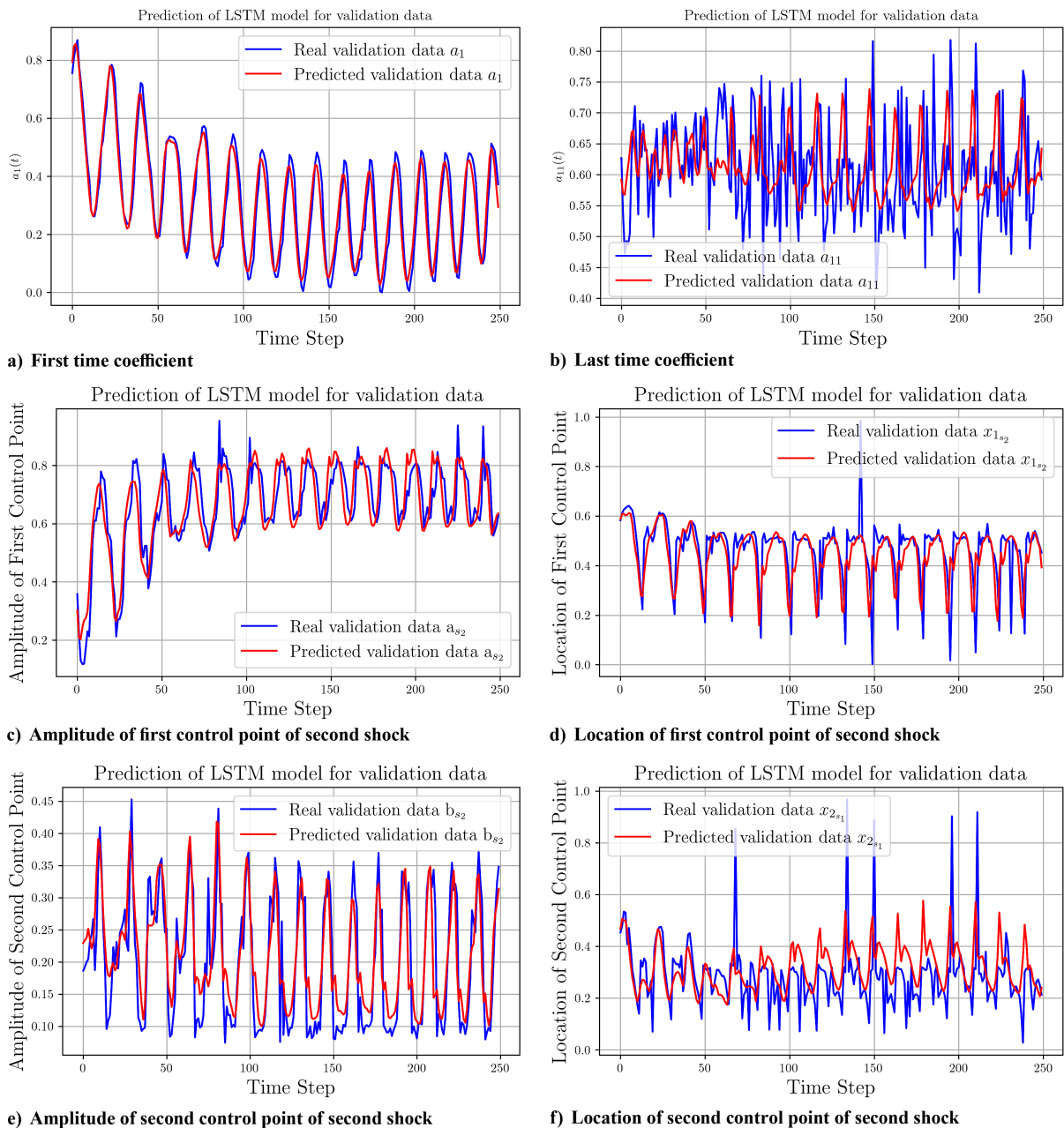

a) **First time coefficient**

b) **Last time coefficient**

c) **Amplitude of first control point of second shock**

d) **Location of first control point of second shock**

e) **Amplitude of second control point of second shock**

f) **Location of second control point of second shock**

Fig. 31   **Normalized validation data.**

model. The second was the neural network time coefficient error, defined as the instantaneous MSE between the actual and predicted enriched reduced-order basis. Finally, the total error of the ROM represents the distance between the full-order pressure distribution and the predicted enriched reduced-order basis generated by the neural network.

Figure 28 displays the three errors for the last 30 time steps of the test data set. The projection error, which measures the discrepancy between the full-order pressure distributions and the actual enriched reduced-order basis, represents the best possible accuracy the neural network can achieve. Essentially, an optimally designed and perfectly trained neural network would exhibit a similar level of error as seen in the projection. Moreover, the neural network time coefficients error and the total error show comparable trends. A maximum error of $6 \cdot 10^{-3}$ occurs at time step 12, while the average error for both comparisons remains below $3 \cdot 10^{-3}$. Furthermore, Fig. 32 illustrates the predicted, projected, and full-order pressure distributions for

Sec. I at selected time steps. These plots demonstrate that, despite using a limited training dataset, the ePOD-LSTM model accurately predicts the true pressure distribution, even in challenging discontinuity locations.

VI. Conclusions

This study explores the use of CFD-based system identification techniques to develop ROMs for predicting aerodynamic loads and surface pressures on a generic fighter configuration at transonic speeds. Two pseudorandom binary sequence (PRBS) training maneuvers were employed, one at a constant Mach number and another with an optimized Mach variation, to generate training data. Various ROM approaches, including regression, feed-forward neural networks, and autoregressive modeling, were used to predict integrated forces and moments, while an ePOD combined with an LSTM network was applied for surface pressure prediction. The

a) t=3.876 s, AoA=12.23°

b) t=3.896 s, AoA=7.64°

c) t=3.900 s, AoA=5.21°

d) t=3.924 s, AoA=10.28°
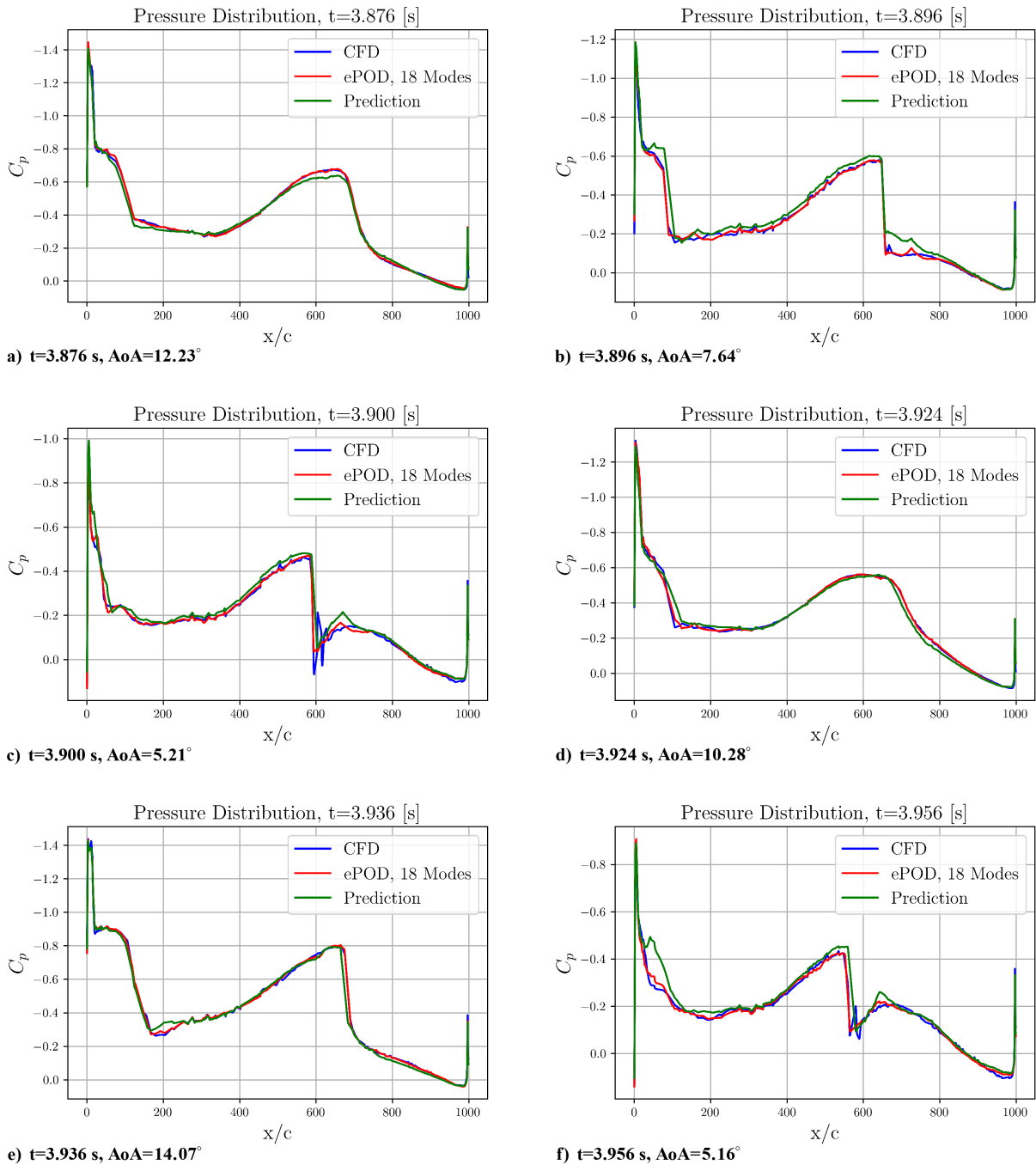
e) t=3.936 s, AoA=14.07°

f) t=3.956 s, AoA=5.16°

Fig. 32 Predicted pressure distribution of section 1 with the ePOD-LSTM ROM.

ePOD method effectively captured pressure discontinuities due to shocks, leading to improved accuracy over standard POD approaches. The models demonstrated good agreement with Kestrel CFD data for both static and dynamic aerodynamic responses, validating their predictive capabilities. Future work will focus on optimizing input signal design, refining neural network training algorithms, and extending ROM techniques to model full flowfield dynamics under varying Mach number conditions.

Acknowledgments

References

[1] Kroll, N., Abu-Zurayk, M., Dimitrov, D., Franz, T., Führer, T., Gerhold, T., Görtz, S., Heinrich, R., Ilic, C., Jepsen, J., et al., "DLR Project Digital-X: Towards Virtual Aircraft Design and Flight Testing Based on High-Fidelity Methods," *CEAS Aeronautical Journal*, Vol. 7, No. 1, 2016, pp. 3–27.
https://doi.org/10.1007/s13272-015-0179-7

[2] Ghoreyshi, M., Jirásek, A., and Cummings, R. M., "Reduced Order Unsteady Aerodynamic Modeling for Stability and Control Analysis Using Computational Fluid Dynamics," *Progress in Aerospace Sciences*, Vol. 71, 2014, pp. 167–217.
https://doi.org/10.1016/j.paerosci.2014.09.001

[3] Ghoreyshi, M., Jirsek, A., and Cummings, R. M., "Computational Investigation into the Use of Response Functions for Aerodynamic Loads Modeling," *AIAA Journal*, Vol. 50, No. 6, 2012, pp. 1314–1327.

[4] Hall, K. C., Thomas, J. P., and Dowell, E. H., "Reduced-Order Modelling of Unsteady Small-Disturbance Using a Frequency-Domain Proper Orthogonal Decomposition Technique," AIAA Paper 1999-0655, Jan. 1999.

[5] Peters, N. J., Wissink, A., and Ekaterinaris, J., "On the Construction of a Mode Based Reduced Order Model for a Moving Store," *Aerospace Science and Technology*, Vol. 123, 2022, Paper 107484.
https://doi.org/10.1016/j.ast.2022.107484

[6] Peters, N., Wissink, A., and Ekaterinaris, J., "Machine Learning-Based Surrogate Modeling Approaches for Fixed-Wing Store Separation," *Aerospace Science and Technology*, Vol. 133, 2023, Paper 108150.
https://doi.org/10.1016/j.ast.2023.108150

[7] Silva, W. A., "Application of Nonlinear Systems Theory to Transonic Unsteady Aerodynamic Responses," *Journal of Aircraft*, Vol. 30, No. 5, 1993, pp. 660–668.
https://doi.org/10.2514/3.46395

[8] Dias Ribeiro, M., Stradtner, M., and Bekemeyer, P., "Unsteady Reduced Order Model with Neural Networks and Flight-Physics-Based Regularization for Aerodynamic Applications," *Computers & Fluids*, Vol. 264, 2023, Paper 105949.
https://doi.org/10.1016/j.compfluid.2023.105949

[9] Stradtner, M., Liersch, C. M., and Bekemeyer, P., "An Aerodynamic Variable-Fidelity Modelling Framework for a Low-Observable UCAV," *Aerospace Science and Technology*, Vol. 107, 2020, Paper 106232.
https://doi.org/10.1016/j.ast.2020.106232

[10] Immordino, G., Da Ronch, A., and Righi, M., "Steady-State Transonic Flowfield Prediction via Deep-Learning Framework," *AIAA Journal*, Vol. 62, No. 5, 2024, pp. 1–17.
https://doi.org/10.2514/1.J063545

[11] Allen, J., and Ghoreyshi, M., "Forced Motions Design for Aerodynamic Identification and Modeling of a Generic Missile Configuration," *Aerospace Science and Technology*, Vol. 77, 2018, pp. 742–754.
https://doi.org/10.1016/j.ast.2018.04.014

[12] Leontaritis, I. J., and Billings, S. A., "Input-Output Parametric Models for Non-Linear Systems Part I: Deterministic Non-Linear Systems," *International Journal of Control*, Vol. 41, No. 2, 1985, pp. 303–328.
https://doi.org/10.1080/0020718508961129

[13] Leontaritis, I. J., and Billings, S. A., "Input-Output Parametric Models for Non-Linear Systems Part II: Stochastic Non-Linear Systems," *International Journal of Control*, Vol. 41, No. 2, 1985, pp. 329–344.
https://doi.org/10.1080/0020718508961130

[14] Glaz, B., Liu, L., and Friedmann, P. P., "Reduced-Order Nonlinear Unsteady Aerodynamic Modeling Using a Surrogate-Based Recurrence Framework," *AIAA Journal*, Vol. 48, No. 10, 2010, pp. 2418–2429.
https://doi.org/10.2514/1.J050471

[15] Ghoreyshi, M., Cummings, R. M., Ronch, A. D., and Badcock, K. J., "Transonic Aerodynamic Load Modeling of X-31 Aircraft Pitching Motions," *AIAA Journal*, Vol. 51, No. 10, 2013, pp. 2447–2464.
https://doi.org/10.2514/1.J052309

[16] Ghoreyshi, M., Jirásek, A., and Cummings, R. M., "Computational Approximation of Nonlinear Unsteady Aerodynamics Using an Aerodynamic Model Hierarchy," *Aerospace Science and Technology*, Vol. 28, No. 1, 2013, pp. 133–144.
https://doi.org/10.1016/j.ast.2012.10.009

[17] Lui, H. F., and Wolf, W. R., "Construction of Reduced-Order Models for Fluid Flows Using Deep Feedforward Neural Networks," *Journal of Fluid Mechanics*, Vol. 872, 2019, pp. 963–994.
https://doi.org/10.1017/jfm.2019.358

[18] Huang, R., Hu, H., and Zhao, Y., "Nonlinear Reduced-Order Modeling for Multiple-Input/Multiple-Output Aerodynamic Systems," *AIAA Journal*, Vol. 52, No. 6, 2014, pp. 1219–1231.
https://doi.org/10.2514/1.J052323

[19] Stradtner, M., Drazen, D., and van Rooij, M., "Introduction to AVT-351: Enhanced Computational Performance and Stability & Control Prediction for NATO Military Vehicles," *AIAA SCITECH 2023 Forum*, AIAA Paper 2023-0820, 2023.
https://doi.org/10.2514/6.2023-0820

[20] O'Neill, C., and Arena, A., "Comparison of Time Domain Training Signals for CFD Based Aerodynamic System Identification," *42nd AIAA Aerospace Sciences Meeting and Exhibit*, AIAA Paper 2004-0209, 2004.
https://doi.org/10.2514/6.2004-209

[21] Pfifer, H., and Danowsky, B. P., "System Identification of a Small Flexible Aircraft-Invited," *AIAA Atmospheric Flight Mechanics Conference*, AIAA Paper 2016-1750, 2016.

[22] Sears, D. R., and Morton, S. A., "HPCMP CREATETM–The Remarkable Success of a DoD Software Factory," AIAA Paper 2023-2014, Jan. 2023.

[23] Galrinho, M., "Least Squares Methods for System Identification of Structured Models," Ph.D. Thesis, KTH Royal Inst. of Technology, Stockholm, Sweden, 2016.

[24] Rasmussen, C. E., and Williams, C. K. I., "Gaussian Processes for Machine Learning," *Adaptive Computation and Machine Learning*. 3rd ed., MIT Press, Cambridge, MA, 2008.

[25] Bekemeyer, P., Bertram, A., Hines Chaves, D. A., Dias Ribeiro, M., Garbo, A., Kiener, A., Sabater, C., Stradtner, M., Wassing, S., Widhalm, M., et al., "Data-Driven Aerodynamic Modeling Using the DLR SMARTy Toolbox," *AIAA Aviation 2022 Forum*, AIAA Paper 2022-3899, 2022.
https://doi.org/10.2514/6.2022-3899

[26] Stradtner, M., and Bekemeyer, P., "Nonlinear Unsteady Aerodynamic Reduced-Order Modeling Using a Surrogate-Based Recurrent Framework," *AIAA Aviation Forum and Ascend 2024*, AIAA Paper 2024-4157, June 2024.
https://doi.org/10.2514/6.2024-4157

[27] Fresca, S., and Manzoni, A., "POD-DL-ROM: Enhancing Deep Learning-Based Reduced Order Models for Nonlinear Parametrized PDEs by Proper Orthogonal Decomposition," *Computer Methods in Applied Mechanics and Engineering*, Vol. 388, 2022, Paper 114181.
https://doi.org/10.1016/j.cma.2021.114181

[28] Mohan, A. T., and Gaitonde, D. V., "A Deep Learning Based Approach to Reduced Order Modeling for Turbulent Flow Control Using LSTM Neural Networks," arXiv preprint arXiv: 1804.09269, 2018.

[29] Catalani, G., "Machine Learning Based Local Reduced Order Modeling for the Prediction of Unsteady Aerodynamic Loads.," MSc. Thesis, Delft Univ. of Technology Delft, Delft, The Netherlands, 2022.

[30] Bourier, S., "Development of a CFD Data-Driven Surrogate Model Using the Neural Network Approach for Prediction of Aircraft Performance Characteristics," MSc. Thesis, Delft Univ. of Technology Delft, Delft, The Netherlands, 2021.

[31] Gallagher, N. B., "Whittaker Smoother," White Paper Eigenvector Research, 2018, www.eigenvector.com.

[32] Kovacs, L., Passaggia, P.-Y., Mazellier, N., and Lago, V., "Detection Method for Shock-Waves in Viscous Flows," *Experiments in Fluids*, Vol. 63, No. 1, 2022, p. 11.
https://doi.org/10.1007/s00348-021-03360-y

[33] Rumelhart, D. E., Hinton, G. E., and Williams, R. J., "Learning Representations by Back-Propagating Errors," *Nature*, Vol. 323, No. 6088, 1986, pp. 533–536.
https://doi.org/10.1038/323533a0

[34] Lipton, Z. C., Berkowitz, J., and Elkan, C., "A Critical Review of Recurrent Neural Networks for Sequence Learning," arXiv preprint arXiv: 1506.00019, 2015.

[35] Brunton, S. L., Noack, B. R., and Koumoutsakos, P., "Machine Learning for Fluid Mechanics," *Annual Review of Fluid Mechanics*, Vol. 52, No. 1, 2020, pp. 477–508.
https://doi.org/10.1146/annurev-fluid-010719-060214

[36] Hochreiter, S., and Schmidhuber, J., "Long Short-Term Memory," *Neural Computation*, Vol. 9, No. 8, 1997, pp. 1735–1780.
https://doi.org/10.1162/neco.1997.9.8.1735

[37] Goodfellow, I., Bengio, Y., and Courville, A., *Deep Learning*, MIT Press, Cambridge, MA, 2016, http://www.deeplearningbook.org.

[38] Gers, F. A., Schmidhuber, J., and Cummins, F., "Learning to Forget: Continual Prediction with LSTM," *Neural Computation*, Vol. 12, No. 10, 2000, pp. 2451–2471.
https://doi.org/10.1162/089976600300015015

[39] Bányász, C., and of Automatic Control, I. F, *Adaptive Systems in Control and Signal Processing 1995: A Postscript Volume from the Fifth IFAC Symposium*, IFAC Series, International Federation of Automatioc Control, Elsevier, 1995, https://books.google.com/books?id=kNVSAAAAMAAJ.

[40] Morelli, E. A., "Multiple Input Design for Real-Time Parameter Estimation in the Frequency Domain," *IFAC Proceedings*, Vol. 36, No. 16, 2003, pp. 639–644.
https://doi.org/10.1016/S1474-6670(17)34833-4

[41] Cummings, R. M., Morton, S. A., and McDaniel, D. R., "Experiences in Accurately Predicting Time-Dependent Flows," *Progress in Aerospace Sciences*, Vol. 44, No. 4, 2008, pp. 241–257.
https://doi.org/10.1016/j.paerosci.2008.01.001

[42] Schütte, A., and Hummel, D., "Numerical Design Studies on the Roll Stability of a Multi-Delta-Wing Configuration," *Journal of Aircraft*, Vol. 60, No. 3, 2022, pp. 1–17.
https://doi.org/10.2514/1.C037128

[43] Rein, M., "Subsonic, Transonic and Supersonic Wind Tunnel Tests of the Generic Slender Wing Configuration DLR-F22 with Leading-Edge Vortex Controllers and Strakes," TR, DLR, 2022, https://elib.dlr.de/185854/.

[44] Liersch, C. M., Schuette, A., Moerland, E., and Kalanja, M., "DLR Project Diabolo: An Approach for the Design and Technology Assessment for Future Fighter Configurations," *AIAA Aviation 2023 Forum*, AIAA Paper 2023-3515, 2023.
https://doi.org/10.2514/6.2023-3515

[45] Farcy, D., Tanguy, G., Vauchel, N., Dubot, G., and Garnier, E., "Static and Dynamic Aerodynamic Coefficients Evaluation on a Generic Fighter Configuration in ONERA Low Speed Wind Tunnels," *AIAA Aviation Forum and Ascend*, AIAA Paper 2024-4066, 2024.
https://doi.org/10.2514/6.2024-4066

[46] Widhalm, M., Stradtner, M., Schuette, A., Ghoreyshi, M., Jirasek, A., and Seidel, J., "Comparison of Reduced Order Models for Evaluating Stability Derivatives for the DLR-F22 ONERA Model," *AIAA Aviation 2023 Forum*, AIAA Paper 2023-4199, June 2023.
https://doi.org/10.2514/6.2023-4199

S. Brunton
Associate Editor